Accepted for publication in "International Journal for Numerical Methods in Fluids" (November 1st, 2015)

A stabilization for three-dimensional discontinuous Galerkin discretizations applied to nonhydrostatic atmospheric simulations

Revised manuscript submitted to IJNMF on Spetember 21, 2015

Sébastien Blaise[a], Jonathan Lambrechts[a], Eric Deleersnijder[b,c]

[a] *Université catholique de Louvain, Institute of Mechanics, Materials and Civil Engineering (IMMC), 4 Avenue Georges Lemaître, B-1348 Louvain-la-Neuve, Belgium*
[b] *Université catholique de Louvain, Institute of Mechanics, Materials and Civil Engineering (IMMC) & Earth and Life Institute (ELI), 4 Avenue Georges Lemaître, B-1348 Louvain-la-Neuve, Belgium*
[c] *Delft University of Technology, Delft Institute of Applied Mechanics (DIAM), Mekelweg 4, 2628CD Delft, The Netherlands*

Abstract

A discontinuous Galerkin nonhydrostatic atmospheric model is used for two- and three-dimensional simulations. There is a wide range of timescales to be dealt with. To do so, two different implicit/explicit time discretizations are implemented. A stabilization, based upon a reduced-order discretization of the gravity term is introduced to ensure the balance between pressure and gravity effects. While not affecting significantly the convergence properties of the scheme, this approach allows the simulation of anisotropic flows without generating spurious oscillations, as it happens for a classical discontinuous Galerkin discretization. This approach is shown to be less diffusive than usual spatial filters. A stability analysis demonstrates that the use of this modified scheme discards the instability associated with the usual discretization.

Validation against analytical solutions is performed, confirming the good convergence and stability properties of the scheme. Numerical results demonstrate the attractivity of the discontinuous Galerkin method with implicit/explicit time integration for large scale atmospheric flows.

Keywords:
discontinuous Galerkin, atmospheric model, Euler equations, geophysical flow, computational fluid dynamics

1. Introduction

Over the last decades, global climate models have been widely used to predict future climate trends. However, climate change will mostly affect the ecosystems and social and economic well-being at the regional scale (IPCC, 1997). Therefore, improving our capabilities in regional atmospheric simulations is of critical importance. Despite the rapid advances in computational power, current global models are not able to represent the multiscale aspects of the climate system (Slingo et al., 2009; Shukla et al., 2009). The advances needed for performing multiscale regional climate simulations will come in part from the development of more efficient numerical algorithms. Similar considerations also apply to numerical weather forecasting, for which a better resolution of local terrain and important small-scale dynamics will be achieved through the use of innovative multiscale techniques (e.g. Gopalakrishnan et al., 2002).

Spatial scales of interest in the atmosphere vary from meters for three-dimensional turbulence to thousands of kilometers for the general circulation. Many different phenomena characterized by different scales, such as thunderstorms (2-20 km) and hurricanes (200-2000 km), lie in this interval (Thunis and Borstein, 1996). While numerical models cannot afford to resolve explicitly the whole range of scales, the recent increases in computational power enabled the resolution of smaller and smaller scales of flows in large scale models. During the past 10 years, the typical grid size in the atmosphere of coupled atmosphere-ocean global models decreased from about 300 km to 25 km (Slingo et al., 2009; McMorrow, 2013).

This resolution is still not sufficient to capture phenomena such as thunderstorms and mesoscale convection, which would need a grid size of order of 1-10 km. Models able to resolve such scales of motion are restricted to a specific region and are usually referred to as regional models. They cannot produce an accurate description of the interaction between regional phenomena and the global scale circulation. Indeed,

energy transfers from the synoptic scale (> 1000 km) to the mesoscale (1-2000 km) act as a forcing to induce mesoscale circulations. For example, large-scale vorticity and temperature advection may facilitate the generation of mesoscale frontal systems (Lin, 2010). The resolution of individual mesoscale processes must be considered in a global context, to encompass the interactions between the different scales. In other words, an accurate regional model must also resolve the global scale of motion.

As a first step toward high-resolution modeling, several studies made the models extremely scalable, while increasing their resolution homogeneously (Dennis et al., 2005; Wehner, 2008; McClean et al., 2011; Palipane et al., 2013). The problem with such approaches is mainly computational. Indeed, each uniform doubling of the horizontal resolution increases the computational cost by about one order of magnitude. The cost of climate or weather simulations is directly correlated with the total number of spatial grid points employed.

New models need to be designed, using more effectively the computational resources than current models do. Emerging numerical techniques have to be used, taking into account the multiscale aspect of the flows. One way to reduce the number of grid points in a model, while preserving the range of spatial scales involved, is to employ fully unstructured meshes, allowing one to increase the resolution exactly when and where needed, thereby giving rise to multi-scale/physics numerical simulations. Well suited to unstructured grids, the continuous finite element method has been proposed to replace the global spectral methods used on structured grids (Taylor et al., 1997; Dennis et al., 2012). However, such methods are not stable for advection-diffusion problems and require additional stabilization mechanisms. The finite volume method does not suffer from this problem and has been chosen to build several atmospheric models (Steppeler et al., 2002; Weller et al., 2009; Machenhauer et al., 2009; Rauscher et al., 2013; Park et al., 2013). To attain high-order accuracy, the variables in an element need to be reconstructed based on the neighboring elements, the reconstruction stencil being wider as the desired order of accuracy increases. As the parallel efficiency of models is highly affected by the amount of communications between nodes, a good scalability of such non-local algorithms is difficult to achieve.

The discontinuous Galerkin (DG) method is a combination of the continuous finite element method and the finite volume method. It can achieve high-order accuracy while using a very compact stencil, the degrees of freedom being local to the elements. This scheme is attractive for atmospheric modeling, where high-order accuracy and parallel efficiency are generally considered desirable. In addition, allowing for precise advection schemes (Cockburn et al., 1999), the DG method is particularly well adapted to atmospheric dynamics, which is dominated by advective processes. Hence, several DG atmospheric models are currently under development (St-Cyr and Neckels, 2009; Nair et al., 2005; Giraldo and Restelli, 2008; Nair et al., 2009; Giraldo et al., 2010; Kelly and Giraldo, 2012; Brdar et al., 2013). While a few DG models simulate geophysical flows on the sphere, they are still in active development, and generally not ready for production runs. The generalization of those models to realistic three-dimensional flows on the sphere is a very challenging task. Given the high increase of the computational load due to three-dimensional elements, parallel efficiency becomes critical but is perfectly compatible with the discontinuous Galerkin method. As an example, Kelly and Giraldo (2012) investigated the scaling properties of the discontinuous Galerkin method for three-dimensional nonhydrostatic atmospheric simulations, demonstrating good scaling up to 32 000 computing cores.

The atmosphere is highly anisotropic, with vertical scales much smaller than horizontal ones. The computational grids used by numerical models usually consist of a certain number of vertical levels, with essentially the same horizontal structure at each layer (Thuburn, 2015). Although the ratio between horizontal and vertical resolutions depends on the scales considered, the vertical grid spacing has to be much smaller than the horizontal one in order to capture the anisotropy (Lindzen and Fox-Rabinovitz, 1989). For large-scale simulations the ratio of horizontal versus vertical resolution is usually around 150-300, while it can decrease towards 1-15 for limited-area fine resolution models (Hamilton, 2008). Models based upon a variable horizontal resolution should be able to handle both moderate and strong anisotropies in the grid. Hence, it is important to rely upon a discretization which is stable, efficient and accurate for this whole range of aspect ratios.

This paper focuses on the implementation and validation of a high-order three-dimensional discontinuous Galerkin model solving the compressible Euler equations. To efficiently handle the wide range of timescales, two different implicit/explicit time discretizations are implemented. Attention is paid to the convergence properties and stability of the model for highly anisotropic meshes encountered in large-scale atmospheric simulations. Due to the discrete incompatibility between the pressure and gravity terms, those simulations may give rise to spurious oscillations if a classical discontinuous Galerkin method is resorted to. To avoid

those artefacts, the vertical discretization of the gravity term is adapted such that its balance with the pressure term can be ensured in the case of a hydrostatic equilibrium.

Section 2 of this article presents the continuous equations solved by the model. Section 3 is devoted to the spatial discretization, including the boundary conditions and the stabilization used to prevent the model from generating spurious oscillations, while section 4 describes the temporal discretization. Dissipation mechanisms are presented in section 5. The last section describes the application of the model on two- and three-dimensional test cases, in order to assess the dissipation mechanisms, the convergence properties and stability of the scheme, its behavior on nonhydrostatic and complex terrain simulations, and its parallel efficiency.

2. Model equations

The model solves the two- and three-dimensional compressible Euler equations, describing non-hydrostatic atmospheric processes. Different formulations of the equations are reviewed by Giraldo and Restelli (2008). According to the latter, the differences between the formulations are rather small. We use the inviscid version of equation set 2, because it is in conservative form. Further, the potential temperature appears directly in the equations, avoiding the need for an extra step when using existing physical parameterizations. Hence, the governing equations read:

$$\frac{\partial}{\partial t}\begin{pmatrix}\rho\\ \rho\mathbf{u}\\ \rho\theta\end{pmatrix}+\begin{pmatrix}\nabla\cdot(\rho\mathbf{u})\\ \nabla\cdot(\rho\mathbf{u}\mathbf{u}+p\mathbb{I})+\rho g\hat{\mathbf{e}}_{\mathbf{z}}\\ \nabla\cdot(\rho\theta\mathbf{u})\end{pmatrix}=0, \tag{1}$$

where ρ is the density, θ is the potential temperature, and $\mathbf{u}=(u,v,w)^T$ is the velocity vector, v being used in three-dimensional configurations only. The gravitational acceleration is denoted g while $\hat{\mathbf{e}}_{\mathbf{z}}$ is a unit vector pointing upwards and $\mathbb{I}=\mathrm{diag}(1,\ldots,1)$ is an identity matrix of size equal to the spatial dimension d. The pressure p in the momentum equation is computed by means of the equation of state

$$p=p_0\left(\frac{\rho\theta R_d}{p_0}\right)^{\frac{c_p}{c_v}}, \tag{2}$$

where p_0 is the reference surface pressure, $R_d=c_p-c_v$ is the gas constant, while c_p and c_v are the specific heat of the air at constant pressure and volume. To allow for a better representation of the hydrostatic balance, we follow the splitting introduced by Giraldo and Restelli (2008):

$$\rho(\mathbf{x},t) = \overline{\rho}(z)+\rho'(\mathbf{x},t), \tag{3a}$$
$$(\rho\theta)(\mathbf{x},t) = \overline{\rho\theta}(z)+(\rho\theta)'(\mathbf{x},t), \tag{3b}$$
$$p(\mathbf{x},t) = \overline{p}(z)+p'(\mathbf{x},t) \qquad \text{with} \qquad \overline{p}=p_0\left(\frac{\overline{\rho\theta}R_d}{p_0}\right)^{\frac{c_p}{c_v}}, \tag{3c}$$

where $\mathbf{x}=(x,y,z)^T$ is the position vector and the background (overlined) values are in hydrostatic balance (i.e. $\frac{\partial\overline{p}}{\partial z}+\overline{\rho}g=0$). The governing equations (1) can then be rewritten as

$$\underbrace{\frac{\partial}{\partial t}\begin{pmatrix}\rho'\\ \rho\mathbf{u}\\ (\rho\theta)'\end{pmatrix}}_{\triangleq\mathbf{q}}+\underbrace{\begin{pmatrix}\nabla\cdot(\rho\mathbf{u})\\ \nabla\cdot(\rho\mathbf{u}\,\mathbf{u}+p'\mathbb{I})+\rho' g\hat{\mathbf{e}}_{\mathbf{z}}\\ \nabla\cdot(\rho\theta\mathbf{u})\end{pmatrix}}_{\triangleq\mathbf{F}}=0. \tag{4}$$

This splitting allows us to trivially satisfy the prescribed background state (i.e. $\rho=\overline{\rho}$, $\rho\theta=\overline{\rho\theta}$, $p=\overline{p}$ and $\rho\mathbf{u}=0$), and reduces the discretization error for any solution close to this background state.

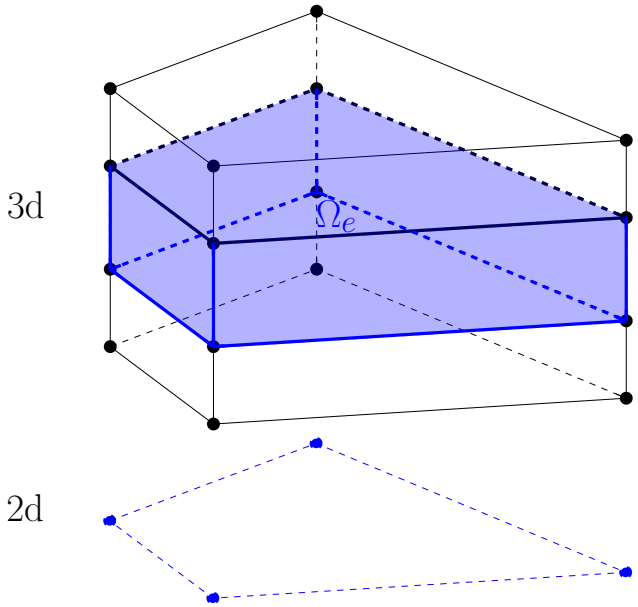

Figure 1: Sketch of a column of hexahedra resulting from the vertical extrusion of a two-dimensional quadrilateral element.

3. Space discretization

3.1. Mesh

The computational domain is split into several elements, which can be either quadrilaterals (2D) or hexahedra (3D). This is not a general restriction of the DG method, but rather a design choice: for such elements, quadrature rules, test and shape functions can be seen as tensor products of their one-dimensional equivalent. Given the large contrast between horizontal and vertical dynamics, the mesh is obtained by extruding over the vertical a horizontal unstructured mesh. Figure 1 shows an example of a single two-dimensional element of a horizontal mesh, which is extruded to form a column of hexahedra. Such a structure allows for different treatments of horizontal and vertical dynamics (Blaise et al., 2010; Comblen et al., 2010). Furthermore, coupling with physics packages, often working as column models, will be greatly facilitated. This is of decisive importance for the future application of the discretization in a global circulation model.

3.2. Weak formulation

The Galerkin weak formulation of the momentum equation is obtained by multiplying equations (4) by a set of test functions and integrating over the elements. Upon doing so, a local problem has to be solved for each element Ω_e and test function ϕ_i:

$$\int_{\Omega_e} \phi_i \frac{\partial \rho'}{\partial t} \,\mathrm{d}\Omega + \int_{\Omega_e} \phi_i \nabla \cdot (\rho \mathbf{u}) \,\mathrm{d}\Omega = 0 \tag{5a}$$

$$\int_{\Omega_e} \phi_i \frac{\partial \rho \mathbf{u}}{\partial t} \,\mathrm{d}\Omega + \int_{\Omega_e} \phi_i \nabla \cdot (\rho \mathbf{u}\ \mathbf{u} + p' \mathbb{I}) \,\mathrm{d}\Omega + \int_{\Omega_e} \phi_i \rho' g \hat{\mathbf{e}}_\mathbf{z} \,\mathrm{d}\Omega = 0 \tag{5b}$$

$$\int_{\Omega_e} \phi_i \frac{\partial (\rho\theta)'}{\partial t} \,\mathrm{d}\Omega + \int_{\Omega_e} \phi_i \nabla \cdot (\rho\theta \mathbf{u}) \,\mathrm{d}\Omega = 0 \tag{5c}$$

The unknowns as well as the test functions belong to a common finite dimensional space, whose definition will be detailed later. The discretization of the prognostic variables ρ', $\rho\mathbf{u}$ and $(\rho\theta)'$ is discontinuous at the boundaries of each element. The DG method couples the local problems (5) through numerical fluxes integrated over the boundaries between the elements. Mimicking the finite volume formulations, we integrate (5) by parts, and the boundary flux $\int_{\Gamma_e} \phi_i \boldsymbol{\mathcal{F}} \cdot \mathbf{n} \,\mathrm{d}\Gamma$, with $\mathbf{n}$ the outward normal vector, appears at the left-hand side as an integral along the interfaces between elements, Γ_e. This flux is the only mechanism that allows information to be passed from one element to the others. It is double-valued, as the variables are

not uniquely defined on the interfaces between elements. The key ingredient of the weak formulation is the manner in which a unique flux $\int_{\Gamma_e} \phi_i \boldsymbol{\mathcal{F}}^* \cdot \mathbf{n} \, \mathrm{d}\Gamma$ is chosen, ensuring the accuracy and stability of the method. Following Nair et al. (2005), we use the local Lax-Friedrichs approximation, defined as

$$\boldsymbol{\mathcal{F}}^* \cdot \mathbf{n} = \frac{1}{2} \left(\left(\boldsymbol{\mathcal{F}}^+ + \boldsymbol{\mathcal{F}}^- \right) \cdot \mathbf{n} - \lambda \left(\mathbf{q}^+ - \mathbf{q}^- \right) \right), \tag{6}$$

where the subscripts - and + correspond to the values of the discontinuous fields respectively at the inner and outer sides of the interface, while $\lambda = \max \left(\sqrt{pc_p / (\rho c_v)} + \|\mathbf{u}\| \right)$ is the maximum value computed from both sides of the propagation speed of the fastest phenomena described by the equations. Introducing the mean $\{S\} = 0.5 \left(S^+ + S^- \right)$ and jump $[S] = 0.5 \left(S^+ - S^- \right)$ operators, the Lax-Friedrichs flux (6) can be writen as $\boldsymbol{\mathcal{F}}^* \cdot \mathbf{n} = \{\boldsymbol{\mathcal{F}}\} - \lambda[\mathbf{q}]$. For each test function ϕ_i and element Ω_e, equations (5) become

$$\int_{\Omega_e} \phi_i \frac{\partial \rho'}{\partial t} \, \mathrm{d}\Omega - \int_{\Omega_e} \nabla \phi_i \cdot \rho \mathbf{u} \, \mathrm{d}\Omega + \int_{\Gamma_e} \phi_i \left(\{\rho \mathbf{u}\} \cdot \mathbf{n} - \lambda[\rho'] \right) \mathrm{d}\Gamma = 0, \tag{7a}$$

$$\begin{aligned} \int_{\Omega_e} \phi_i \frac{\partial \rho \mathbf{u}}{\partial t} \, \mathrm{d}\Omega - \int_{\Omega_e} \nabla \phi_i \cdot \left(\rho \mathbf{u} \, \mathbf{u} + p' \mathbb{I} \right) \mathrm{d}\Omega \\ + \int_{\Gamma_e} \phi_i \left(\left(\{\rho \mathbf{u} \, \mathbf{u}\} + \{p'\} \mathbb{I} \right) \cdot \mathbf{n} - \lambda[\rho \mathbf{u}] \right) \mathrm{d}\Gamma = \int_{\Omega_e} -\phi_i \rho' g \hat{\mathbf{e}}_{\mathbf{z}} \, \mathrm{d}\Omega, \end{aligned} \tag{7b}$$

$$\int_{\Omega_e} \phi_i \frac{\partial (\rho\theta)'}{\partial t} \, \mathrm{d}\Omega - \int_{\Omega_e} \nabla \phi_i \cdot (\rho\theta \mathbf{u}) \, \mathrm{d}\Omega + \int_{\Gamma_e} \phi_i \left(\{\rho\theta \mathbf{u}\} \cdot \mathbf{n} - \lambda[(\rho\theta)'] \right) \mathrm{d}\Gamma = 0. \tag{7c}$$

3.3. Discrete formulation

The discrete formulation is obtained by using a DG polynomial approximation for the solution over each element:

$$\mathbf{q}^{\mathbf{h}} = \sum_{j=0}^{n-1} \mathbf{Q}_j \phi_j, \tag{8}$$

where n is the number of shape functions ϕ_j in the element. Following the usual Galerkin procedure, test functions ϕ_i have been selected belonging to the same space as the polynomial basis functions used to approximate the solution (Karniadakis and Sherwin, 2005; Hesthaven and Wartburton, 2008). $\mathbf{Q}_j$ indicates the discrete degrees of freedom corresponding to the prognostic variables $\mathbf{q}$, associated with the shape function of the corresponding index ϕ_j. Following a nodal approach, the shape functions are obtained using the product, for each dimension, of a Lagrange interpolation polynomial L_k of degree k ranging from 0 to P. Some main advantages of the nodal basis are simpler interpolation procedures, as well as the possibility to interpolate the solution at the interface between elements using the element boundary nodes only, leading to a more compact stencil for the interface terms. The three-dimensional shape functions read

$$\phi_j(x, y, z) = L_k(x) L_l(y) L_m(z) \qquad \text{with} \qquad j = k + (P+1)l + (P+1)^2 m, \tag{9}$$

resulting in $n = (P+1)^3$ shape functions. The integrals are performed numerically using a product of one-dimensional Gauss-Legendre quadrature rules.

The Lagrange polynomials have been constructed for a set of equidistant points spanning the element (see Süli and Mayers (2003) for more details and the method to construct the polynomials). This node distribution will facilitate a further model coupling with physics packages. Note that high-order equidistant interpolation is subject to oscillations associated with Runge's phenomenon (Runge, 1901). Yet, those oscillations were not found to be significant for the relatively low polynomial orders considered in this study. It is also possible to use Lagrange polynomials with roots at the Gauss-Legendre or Legendre-Gauss-Lobatto quadrature points, allowing to bypass the interpolation between the nodes and quatrature points (Karniadakis and Sherwin, 2005; Blaise and St-Cyr, 2012). However, the gain resulting from such a configuration is reduced when

some terms of the equations depend on the gradient of the solution (e.g. diffusion terms). In this case, an interpolation is still necessary to compute the gradient. Further, the use of this technique prevents any control over the accuracy of the integration in space: with $P+1$ nodes, the GL quadrature rule integrates exactly polynomials of order $(2P+1)$ while the LGL rule only integrates exactly polynomials of order $(2P-1)$. When performing simulations on the sphere or on curved elements, those techniques result in an underintegration in space.

3.4. Stabilization

When testing the model, strong spurious oscillations affecting the simulations were observed in the case of strongly anisotropic meshes (see section 6.1 for numerical results). The oscillations grew continuously, leading eventually to a model crash. The use of the alternative strong form (Hesthaven and Wartburton, 2008), obtained by performing a second integration by parts on (7), produces results which are slightly different, but also affected by those strong oscillations (not shown). It can be inferred that the instabilities are not caused by an underintegration in space (aliasing). The source of the oscillations can be found by analyzing the governing equations (4), particularly the equation related to the variable ρw which can be written as

$$\frac{\partial \rho w}{\partial t} + \nabla \cdot (\rho \mathbf{u} w) + \frac{\partial p'}{\partial z} + \rho' g = 0. \tag{10}$$

Its last two terms, related to the pressure and gravity effects, are by definition balanced in the case of the hydrostatic equilibrium. This balance must be preserved in the discrete equations, in order to avoid the generation of spurious motions (Botta et al., 2004). However, those terms do not share the same discretization space: the pressure term is obtained from a gradient, which is of order $P-1$ for a spatial approximation of order P. On the other side, the contribution of gravity is expressed as a source term whose degree is P. This discrepancy alters significantly the balance between the two terms, with the effect of producing spurious oscillations.

In order to deal with this incompatibilty, the gravity term is projected into a space whose vertical discrete polynomial order is $P-1$. This order reduction can be performed through the use of a Legendre basis. Following equation (8), the discrete approximation of the prognostic variables is a linear combination of basis functions based on Lagrange polynomials. The exact equivalent approximation can be found based on Legendre polynomials:

$$\mathbf{q}^{\mathbf{h}} = \sum_{j=0}^{n-1} \mathbf{Q}_j^{\mathrm{Le}} \phi_j^{\mathrm{Le}}, \tag{11}$$

where the Le superscript refers to the Legendre basis functions obtained using

$$\phi_j^{\mathrm{Le}}(x,y,z) = L_k^{\mathrm{Le}}(x) L_l^{\mathrm{Le}}(y) L_m^{\mathrm{Le}}(z) \qquad \text{with} \qquad j = k + (P+1)l + (P+1)^2 m, \tag{12}$$

where L_k^{Le} is the Legendre polynomial of degree k. The Legendre polynomials have the advantage of forming a hierarchical basis, whose order can be easily decreased by dropping the highest degree components. Combining (11) and (12), it is possible to restrict the space describing the vertical dimension to a lower polynomial degree:

$$\mathbf{q}^{\mathbf{h}} = \sum_{k=0}^{P}\sum_{l=0}^{P}\sum_{m=0}^{P} \mathbf{Q}_j^{\mathrm{Le}} L_k^{\mathrm{Le}}(x) L_l^{\mathrm{Le}}(y) L_m^{\mathrm{Le}}(z) \simeq \mathbf{q}^{\mathbf{h}*} = \sum_{k=0}^{P}\sum_{l=0}^{P}\sum_{m=0}^{P-1} \mathbf{Q}_j^{\mathrm{Le}} L_k^{\mathrm{Le}}(x) L_l^{\mathrm{Le}}(y) L_m^{\mathrm{Le}}(z) \tag{13}$$

If the source term related to gravity in (10) is computed using $\mathbf{q}^{\mathbf{h}*}$ instead of $\mathbf{q}^{\mathbf{h}}$, the degree of the polynomial basis describing the discretization space over the vertical will be reduced by one. Such a reduction of the polynomial degree has a stabilizing effect on simulations that were unstable using the original discretization, preventing the oscillations to appear. This effect is confirmed by a stability analysis, demonstrating that the reduction of the polynomial degree discards unstable modes from the discrete spatial operator (see Section 6.1).

This local projection of the gravity term has no effect on mass conservation, which is still ensured up to machine precision (Blaise et al., 2015). The computational overhead, resulting only from the local projection operator, is below 5 percents of the total computational time.

3.5. Boundary conditions

Four types of boundary conditions are available. When possible, boundary conditions are weakly imposed by setting appropriate exterior values for the variables when computing the Lax-Friedrichs flux (6) at a boundary edge. However sponge layers are used when needed to guarantee the stability of the model and the absence of spurious reflections.

- The free-slip (wall) boundary condition is implemented by weakly imposing in (6) exterior values of the variables which are mirrored from the interior values:

$$\rho'^{+} = \rho'^{-}, \tag{14a}$$

$$\rho\mathbf{u}^{+} = \rho\mathbf{u}^{-} - 2\left(\rho\mathbf{u}^{-}\cdot\mathbf{n}\right)\mathbf{n}, \tag{14b}$$

$$(\rho\theta)'^{+} = (\rho\theta)'^{-}. \tag{14c}$$

- The exterior value boundary condition is imposed similarly by replacing the right-hand side of (14) with the desired values.

- Periodic boundary conditions are imposed by replacing the right-hand side of (14) with the values taken from corresponding boundary at the opposite side of the domain.

- When strong damping is needed, sponge layers are used. In a sponge layer, an additional source term $\mathbf{S}$ is added to the right-hand side of equations (7) to relax the variables towards a prescribed value $\mathbf{q^P}$:

$$\mathbf{S} = \int_\Omega \phi_i \tau \left(\mathbf{q^h} - \mathbf{q^P}\right) \,\mathrm{d}\Omega \tag{15}$$

  with a damping coefficient inspired from Durran and Klemp (1983):

$$\tau = -\frac{\alpha}{2}\left(1 + \cos\left(-\frac{\min(d_b\ ,\ w_b)}{w_b}\pi\right)\right), \tag{16}$$

  where d_b is the distance from the boundary. The parameter α, as well as the sponge layer width w_b, has to be tuned to fit the flow configuration and resolution.

4. Time discretization

The implicit/explicit Runge-Kutta methods (IMEX) are a trade-off between explicit and implicit Runge-Kutta methods. On the one hand, explicit methods require a small time step. On the other hand, fully implicit methods need the solution of large nonlinear systems, making them very expensive in terms of memory, CPU time and parallel communications for large three-dimensional applications. Because of the different temporal scales involved, the IMEX time discretization developed by Ascher et al. (1995, 1997) is a good candidate for the equations (4), applied to the simulation of compressible flows (Restelli and Giraldo, 2009; Dolejší and Feistauer, 2004). In standard atmospheric configurations, the acoustic waves are the fastest phenomena, with a propagation speed of about 350 ms^{-1}. This high celerity restricts the explicit time step to a small value due to the CFL stability condition. However, acoustic waves are generally not an important phenomena for modelers, who are more interested in advective timescales. The IMEX method allows to circumvent the CFL condition by treating the linear acoustic waves implicitly, while the remaining terms are explicit. Following Giraldo et al. (2010), to apply IMEX integration, the right-hand side of (4) is additively split into a linear part responsible for the acoustic waves and a nonlinear part. The linear terms

$$\mathbf{F}_{\mathrm{IM}} = \begin{pmatrix} \nabla\cdot(\rho\mathbf{u}) \\ \nabla\cdot(p'_{\mathrm{IM}}\mathbb{I}) + \rho' g\hat{\mathbf{e}}_\mathbf{z} \\ \nabla\cdot\left(\overline{\theta}\rho\mathbf{u}\right) \end{pmatrix}, \tag{17}$$

with the pressure linearized as

$$p'_{\mathrm{IM}} = \frac{\gamma\overline{p}}{\overline{\rho\theta}}(\rho\theta)', \tag{18}$$

are solved implicitly, while the remaining part $\mathbf{F}_{\mathrm{EX}} = \mathbf{F} - \mathbf{F}_{\mathrm{IM}}$ is solved explicitly. The acoustic waves being damped by the implicit scheme, the time step is only limited by the advection scale. One advantage of this splitting is that a single linear system has to be solved at each Runge-Kutta step. In contrast, the fully implicit approach requires the solution of a nonlinear system at each step, which is performed by solving several linear systems (e.g. one for each Newton-Raphson iteration). But its main asset is the constantness of the system matrix, allowing the preconditioning/factorization to be performed only once. As an example, when a LU factorization is possible, this technique leads to important savings in computational time since the system can be solved at each step using fast forward/backward substitutions.

Despite its interesting properties, the splitting (17-18) still requires the solution of a global linear system. For large three-dimensional problems, this solution is CPU and memory intensive. If parallel computing is considered, the system is distributed over several processors, affecting the parallel performance. Giraldo et al. (2010) proposed another splitting, taking advantage of the anisotropy characteristics of usual large scale atmospheric simulations. The idea is to treat implicitly the linear vertical terms (hence filtering vertical fast waves), while the remaining part is explicit:

$$\mathbf{F}_{\mathrm{IM}} = \begin{pmatrix} \dfrac{\partial \rho w}{\partial z} \\ \left(\dfrac{\partial p'_{\mathrm{IM}}}{\partial z} + \rho' g \right) \hat{\mathbf{e}}_{\mathbf{z}} \;\; s \\ \dfrac{\partial \overline{\theta} \rho w}{\partial z} \end{pmatrix}, \tag{19}$$

with w being the vertical component of $\mathbf{u}$. Equations (19) describe a one-dimensional problem. It is solved using the classical three-dimensional discretization, with some modifications performed to make it equivalent to a one-dimensional vertical discretization. First, when resolving the implicit part (19), each horizontal component of the normal vector is set equal to zero while its vertical component n_z remain unchanged: $\mathbf{n} = (0, 0, n_z)$. Additionally, the Lax-Friedriechs flux (6) is rewritten for the implicit part as:

$$\boldsymbol{\mathcal{F}}^* \cdot \mathbf{n} = \frac{1}{2} \left(\left(\boldsymbol{\mathcal{F}}^+ + \boldsymbol{\mathcal{F}}^- \right) \cdot \mathbf{n} - \lambda \left(\mathbf{q}^+ - \mathbf{q}^- \right) (\mathbf{n} \cdot \mathbf{n}) \right) \tag{20}$$

to remove any horizontal contribution, the latter being included in the explicitly treated part of the equations $\mathbf{F}_{\mathrm{EX}} = \mathbf{F} - \mathbf{F}_{\mathrm{IM}}$.

The time step is then limited by the fast acoustic waves in the horizontal direction and the slow advective scale in the vertical direction. The elements being usually much wider than tall, it is possible to obtain a similar time step restriction for horizontal and vertical dynamics.

Atmospheric simulations have been performed using several different resolutions, and the choice of the time integration method is related to the considered application. We can consider the grid corresponding to a typical global model, as mentioned by Hamilton (2008): 300 km horizontal resolution and 1 km vertical resolution. With acoustic waves propagation speed of 350 ms^{-1} and typical horizontal and vertical wind speeds of respectively 50 ms^{-1} and 1 ms^{-1}, it is possible to compare the estimation of the maximum stable time steps associated with different time discretizations (Table 1). The IMEX method with linear vertical terms implicit (IMEX V) is limited to a time step which is only slightly smaller than the one associated with the IMEX method with linear implicit terms (IMEX HV). Note that several global circulation models rely on a vertical resolution which is drastically increased in the planetary boundary layer. With such models, the time step is clearly not affected by the explicit horizontal dynamics, since the limiting phenomena are the vertical advective terms (Table 1). The IMEX V method has several advantages. Thanks to the absence of horizontal coupling, there is no global linear system to solve, but many small systems, each one being associated with a column of elements. Those small systems can be solved efficiently without requiring excessive memory, e.g. using a direct solver based upon a factorization performed only once at the beginning of the simulation. If the mesh is partitioned in such a way that each column of elements belongs to the same process, the systems are not distributed, reducing the communication costs. Those properties make the IMEX V splitting very appealing for large three-dimensional atmospheric simulations.

The IMEX time integration scheme used in this study is the so-called ARS(2,2,2) method, developed by Ascher et al. (1997). To advance the solution $\mathbf{q}^{\mathbf{h}}_{\mathbf{n-1}}$ at time t_{n-1} to its value $\mathbf{q}^{\mathbf{h}}_{\mathbf{n}}$ at time $t_{n-1} + \Delta t$,

	$\Delta t^{\mathrm{H}}_{\max} = \frac{\Delta x^H}{c^H}$	$\Delta t^{\mathrm{V}}_{\max} = \frac{\Delta x^V}{c^V}$	$\Delta t_{\max} = \min(\Delta t^{\mathrm{H}}_{\max}, \Delta t^{\mathrm{V}}_{\max})$
Explicit	857 s	2.86 s (0.286 s)	2.86 s (0.286 s)
IMEX HV	6000 s	1000 s (100 s)	1000 s (100 s)
IMEX V	857 s	1000 s (100 s)	857 s (100 s)

Table 1: Estimation of the maximum stable time step associated with the explicit time discretization, IMEX method with linear terms implicit (IMEX HV), and IMEX method with linear vertical terms implicit (IMEX V). The propagation speed of the fastest explicitly treated phenomena in the horizontal and vertical directions are respectively called c^H and c^V. The grid size is taken from the example of Hamilton (2008), while the values between parenthesis consider a vertical resolution of 100 meters near the ground.

intermediate states $\mathbf{q^h_{(i)}}$ need to be computed at different sub-steps i. Then, the final solution is recovered using those sub-step states:

$$\mathbf{q^h_{(i)}} = \mathbf{q^h_{n-1}} + \Delta t \sum_{j=1}^{i} a_{i,j} \mathbf{F}_{\mathrm{IM}}(\mathbf{q^h_{(j)}}, t_{n-1} + c_j \Delta t) + \Delta t \sum_{j=1}^{i-1} \hat{a}_{i,j} \mathbf{F}_{\mathrm{EX}}(\mathbf{q^h_{(j)}}, t_{n-1} + \hat{c}_j \Delta t) \tag{21}$$

$$\mathbf{q^h_n} = \mathbf{q^h_{n-1}} + \Delta t \sum_{i=1}^{s} b_i \mathbf{F}_{\mathrm{IM}}(\mathbf{q^h_{(i)}}, t_{n-1} + c_i \Delta t) + \Delta t \sum_{i=1}^{s} \hat{b}_i \mathbf{F}_{\mathrm{EX}}(\mathbf{q^h_{(i)}}, t_{n-1} + \hat{c}_i \Delta t). \tag{22}$$

with $\mathbf{q^h_{(0)}} = \mathbf{q^h_{n-1}}$. For the particular ARS(2,2,2) scheme, $s = 3$ and the coefficients are written as a double Butcher tableau, in which the hats notation refers to the explicit part of the scheme:

$$\begin{array}{c|c} \mathbf{c} & \mathbf{a} \\ \hline & \mathbf{b} \end{array} = \begin{array}{c|ccc} 0 & 0 & 0 & 0 \\ \gamma & 0 & \gamma & 0 \\ 1 & 0 & 1-\gamma & \gamma \\ \hline & 0 & 1-\gamma & \gamma \end{array} \quad \text{and} \quad \begin{array}{c|c} \hat{\mathbf{c}} & \hat{\mathbf{a}} \\ \hline & \hat{\mathbf{b}} \end{array} = \begin{array}{c|ccc} 0 & 0 & 0 & 0 \\ \gamma & \gamma & 0 & 0 \\ 1 & \delta & 1-\delta & 0 \\ \hline & \delta & 1-\delta & 0 \end{array}, \tag{23}$$

with $\gamma = 1 - \frac{\sqrt{2}}{2}$, $\delta = 1 - \frac{1}{2\gamma}$. This scheme has been chosen because of its property to be stiffly accurate and strong stability preserving. Note that several alternatives to ARS IMEX are available. In a recent article, Weller et al. (2013) analyzed different IMEX Runge-Kutta schemes for horizontally explicit, vertically implicit solutions of atmospheric models, including some schemes from Ascher et al. (1997). However, ARS(2,2,2) was not part of the tested methods.

5. Dissipation mechanisms

Dissipation is an inevitable ingredient for a practical atmospheric model. It generally serves two purposes. The first one is to parametrize some unresolved physical phenomena which are not described either because of inaccurate equations or a too coarse resolution. This parametrization takes the form of a diffusion operator, which is added to the equations. The second pourpose of dissipation is stability: numerical methods with low dissipation, such as high-order finite element methods, are likely to produce strong Gibbs oscillations in the presence of shocks or unresolved flows. Several techniques can be used to prevent those oscillations, such as limiters (e.g. Cockburn and Shu, 1998b; Krivodonova, 2007) or a diffusion operator with a non-constant artificial viscosity coefficient (e.g. Persson and Peraire, 2006). The impact of such filters should be minimal in smooth and well-resolved areas. The design of stable and high-order accurate stabilization mechanisms is a difficult task, especially in the case of a (semi-)implicit discretization, and is the focus of intense reseach. In this work, two dissipation mechanisms are considered: a diffusion operator, and a filter designed by Boyd (1996), which is often reffered to as the Boyd-Vandeven filter, and has already been used in atmospheric modeling (e.g. Giraldo and Restelli, 2008; Lauritzen et al., 2011). Both methods are independent and compatible with the stabilization described in section 3.4.

5.1. Diffusion operator

In the realm of discontinuous Galerkin methods, various discretizations of the Laplacian operator exist (see Arnold et al. (2002) for a review). Two of them are especially popular: the Interior Penalty (IP) methods (Arnold, 1982; Riviere, 2008) and the local-DG method (Cockburn and Shu, 1998a).

To accurately handle the diffusion terms without adding any equation to the system, we resort to the IP technique. Following the usual discontinuous Galerkin method (see section 3), the weak form $\mathbf{D}$ of the diffusion operator $\boldsymbol{\nabla} \cdot \kappa \boldsymbol{\nabla} c$ for any variable c and diffusivity coefficient κ can be obtained by multiplying this operator with a test function and integrating the resulting product over each element. Integrating by parts and choosing the mean values at the interfaces yields:

$$\mathbf{D} = \int_{\Gamma_e} \phi_i \left\{ \kappa \boldsymbol{\nabla} c \right\} \cdot \boldsymbol{n} \, \mathrm{d}\Gamma - \int_{\Omega_e} \boldsymbol{\nabla} \phi_i \cdot \kappa \boldsymbol{\nabla} c \, \mathrm{d}\Omega. \tag{24}$$

Choosing the mean values at the interface seems natural for an elliptic operator where the information propagates along all directions. However, such a simple and intuitive treatment of the Laplacian operator is incomplete. Indeed, the jump of the variables at the interfaces between elements is not taken into account by the diffusion operator, even though it is part of the fields variability. In order to complete the discrete formulation, the IP Method consists in adding a penalty term on the discontinuities of the field at the inter-element interfaces

$$\mathbf{D} = \int_{\Gamma_e} \phi_i \left\{ \kappa \boldsymbol{\nabla} c \right\} \cdot \boldsymbol{n} \, \mathrm{d}\Gamma + \int_{\Gamma_e} \phi_i \left\{ \kappa \right\} \mu \left[c \right] \, \mathrm{d}\Gamma - \int_{\Omega_e} \boldsymbol{\nabla} \phi_i \cdot \kappa \boldsymbol{\nabla} c \, \mathrm{d}\Omega = 0, \tag{25}$$

where μ is a penalty parameter scaled in such a way that $\mu \left[c \right]$ is a term similar to a gradient, at the interface level. In other words, $1/\mu$ has to be a suitable length scale. There is a lower bound on μ that ensures optimal convergence. This bound must be as tight as possible, as the larger the value of μ, the worse the conditioning of the operator. Shahbazi (2005) suggests to use the following formula:

$$\mu = \left[\frac{2(P+1)(P+d)}{d} \frac{A(\Gamma_{ef})}{V(\Omega_e, \Omega_f)} \right], \tag{26}$$

where $A(\Gamma_{ef})$ is the area of the interface Γ_{ef} between two considered elements Ω_e and Ω_f, and $V(\Omega_e, \Omega_f)$ is the mean volume of those elements.

5.2. Boyd-Vandeven filter

Based on the Legendre approximation of the variable fields $\mathbf{q^h}$ for a three-dimensional configuration (13), and following the idea of Boyd (1996), it is possible to obtain a smoother approximation of the prognostic variables $\mathbf{q^{h'}}$ using a filtered partial sum:

$$\mathbf{q^h} = \sum_{k=0}^{P} \sum_{l=0}^{P} \sum_{m=0}^{P} \mathbf{Q}_j^{\mathrm{Le}} L_k^{\mathrm{Le}}(x) L_l^{\mathrm{Le}}(y) L_m^{\mathrm{Le}}(z) \simeq \mathbf{q^{h'}} = \sum_{k=0}^{P} \sum_{l=0}^{P} \sum_{m=0}^{P} \mathbf{Q}_j^{\mathrm{Le}} \sigma_k L_k^{\mathrm{Le}}(x) \sigma_l L_l^{\mathrm{Le}}(y) \sigma_m L_m^{\mathrm{Le}}(z), \tag{27}$$

with

$$\sigma_i = \frac{1}{2} \mathrm{erfc} \left(2\sqrt{P} \left(|\delta_i| - \frac{1}{2} \right) \sqrt{ - \frac{\log \left(1 - 4 \left(\delta_i - \frac{1}{2} \right)^2 \right)}{4 \left(\delta_i - \frac{1}{2} \right)^2} } \right), \tag{28}$$

and

$$\delta_i = \begin{cases} 1 & \text{for } i < s, \\ \frac{i-s}{P+1-s} & \text{for } i \geq s. \end{cases} \tag{29}$$

The complementary error function in (27) is defined as

$$\mathrm{erfc}(z) = \frac{2}{\sqrt{\pi}} \int_z^{\infty} e^{-\zeta^2} \, \mathrm{d}\zeta. \tag{30}$$

A parameter s is introduced such that the filter only acts on the components of higher polynomial orders. To limit the filter effect, the final approximation of the solution $\mathbf{q^{h''}}$ is taken as a combination of the original unfiltered approximation and the filtered one, introducing an additional parameter η whose value is between 0 and 1:

$$\mathbf{q^{h''}} = \mathbf{q^h}(1 - \eta) + \mathbf{q^{h'}} \eta. \tag{31}$$

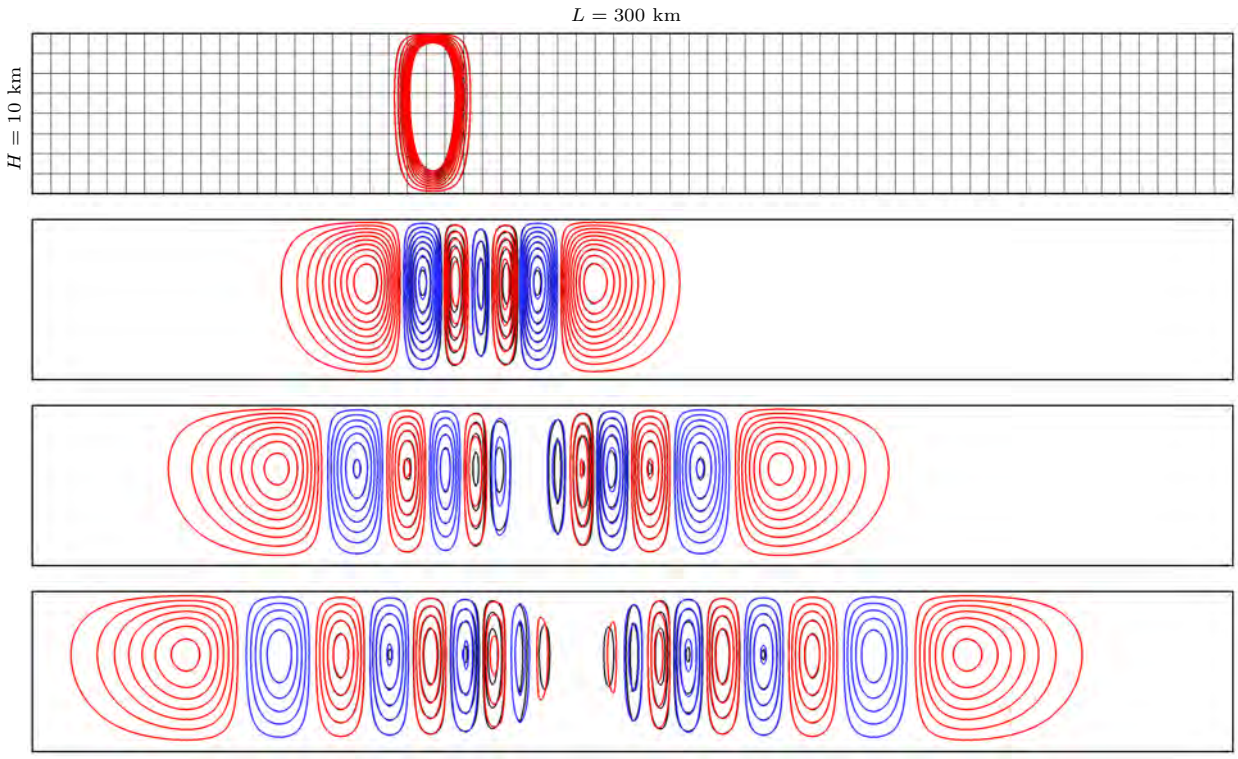

Figure 2: Gravity waves: potential temperature deviation θ' after 0, 10, 20 and 30 minutes (from top to bottom). Contour lines every 0.0005 K from -0.005 K to 0.005 K, without the zero contour, for the model simulation (blue negative, red positive) and analytical solution (black). The solution was computed using third-order polynomials on 64×8 elements. For visualization purposes, the domain is vertically stretched by a factor of 4. As the model solution is close to the analytical solution, the difference between them is only visible for the largest times (lower panels).

6. Numerical results

The model has been successfully applied on different test cases, in order to assess the dissipation mechanisms, the convergence properties and stability of the scheme, its behaviour on nonhydrostatic simulations and in the presence of complex terrain. A reference surface pressure $p_0 = 10^5$ Pa has been considered for all the benchmarks described in this section.

6.1. Two-dimensional gravity waves

For a polynomial order P, the expected order of convergence is $P + 1$. To check numerically that the model reproduces this theoretical order, we resort the gravity waves test case from Baldauf and Brdar (2013), described in Appendix A. It consists of a channel in which gravity waves are triggered by an initial perturbation of the potential temperature in the form of a warm bubble. The waves then propagate along the axis of the channel (Figures 2 and 3).

We consider the spatial and temporal convergences of the L_2 error on the domain Ω, defined as

$$L_2(q_i^h) = \sqrt{\frac{\int_\Omega \left(q_i^h - q_i\right)^2 \, \mathrm{d}\Omega}{\int_\Omega q_i^2 \, \mathrm{d}\Omega}}, \tag{32}$$

where q_i and q_i^h are the components corresponding to each field of the exact solution $\mathbf{q}$ and its approximation $\mathbf{q^h}$. For a spatial discretization of order P, explicit Runge-Kutta time integration methods of the same order P are used, with a time step chosen sufficiently small for the spatial error to be dominant. When the resolution is sufficient to attain the convergence zone, the model exhibits a convergence rate of about $P + 1$

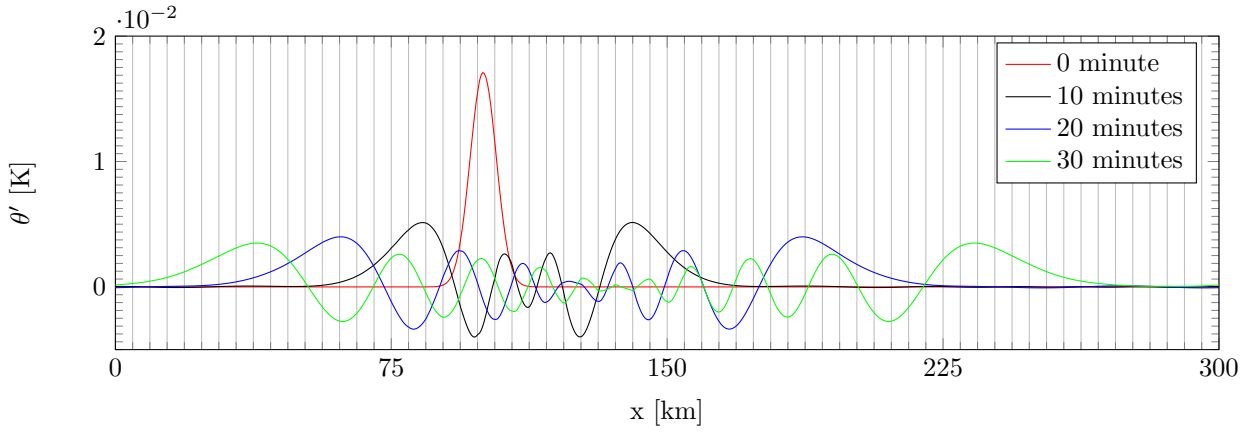

Figure 3: Gravity waves: potential temperature deviation θ' after 0, 10, 20 and 30 minutes. The figure displays profiles at mid-height $z = 5\ 000$ m.

for a polynomial order P (Figure 4). Some convergence rates are even higher than $P + 1$, which is probably related to the superconvergence properties of the discontinuous Galerkin method (Adjerid and Baccouch, 2007).

Based on those convergence results, the spatial discretization seems optimal. However, stability issues were noticed for larger scale anisotropic simulations over longer periods of time. As an illustration, we consider the gravity waves test case for which the horizontal dimension (domain length, bubble width and position) has been multiplied by 80 (Figure 5a: $L = 24\ 000$ km, $x_c = 8\ 000$ km and $d = 400$ km). Using 64×8 elements, the elements are stretched horizontally, leading to a ratio of horizontal versus vertical resolutions of 300 and approximate horizontal and vertical resolutions ($\simeq \frac{\Delta x}{P}$ and $\frac{\Delta z}{P}$) of 125 km and 417 m. This anisotropy corresponds to the example, already discussed in the previous section, of the typical grid of a global model mentioned by Hamilton (2008).

The flow is expected to behave similarly as in the isotropic case, i.e. the propagation of the wave along the axis of the channel. However, the solution is affected by strong oscillations (Figure 5b). Those oscillations grow continuously, leading to a model crash. As explained in Section 3.4, this behaviour is attributed to the imbalance between the vertical pressure gradient and gravity effect in the vertical momentum equation. A modified treatment of the gravity term, based upon a reduction of the polynomial degree associated with the vertical discretization, has been proposed. With this reduction of the polynomial degree, the simulation of gravity waves in an anisotropic domain produces the expected results without any spurious oscillation (Figure 5c).

Those results are supported by a linear stability analysis. Considering a discrete linear spatial operator $\mathbf{A}$, the evolution of the associated solution $\mathbf{q}$ in continuous time reads

$$\frac{\partial \mathbf{q}}{\partial t} = \mathbf{A}\mathbf{q}. \tag{33}$$

The system is considered unstable if the spectrum of $\mathbf{A}$ contains at least one eigenvalue with positive real part (Teschl, 2012). The Euler equations (4) being nonlinear, it is not possible to perform directly a linear stability analysis. Two linear operators are considered as approximations of this nonlinear system: the linear equations used for the implicit part of the IMEX method (17), and the complete equations (4) linearized around the initial condition. The eigenvalues have been computed for the spatial discretization of those two linear operators. To reduce the computational time needed to extract the eigenvalues, the horizontal domain is restricted to the eight columns of hexahedra surrounding the bubble: 5 000 km $<$ x $<$ 11 000 km, with periodic lateral boundaries. As can be seen in Figure 6, the spectrum of the two operators contains eigenvalues whose real part is positive when the regular gravity term is resorted to, indicating an unstable spatial operator. Note that the use of the nonlinear equations exacerbates the instability, which can be seen by the presence of eigenvalues with larger positive real parts. However, in both cases, the use of the reduced-order gravity term results in a displacement of the eigenvalues with positive real part towards the negative side of the real axis, rendering the unstable scheme stable.

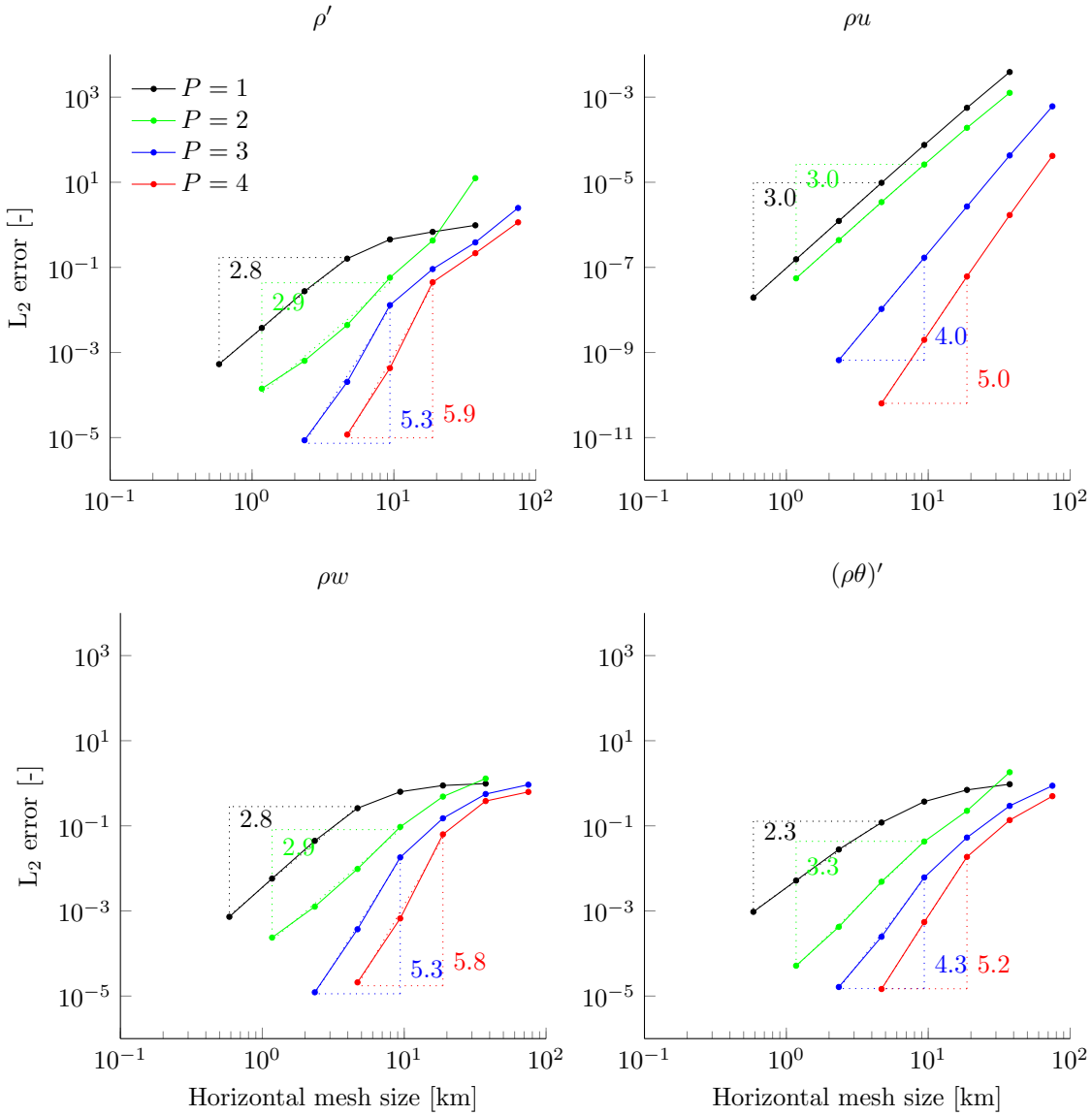

Figure 4: Gravity waves: spatial convergence of the L_2 error after 30 minutes for the prognostic variables, using spatial polynomial orders P from 1 to 4.

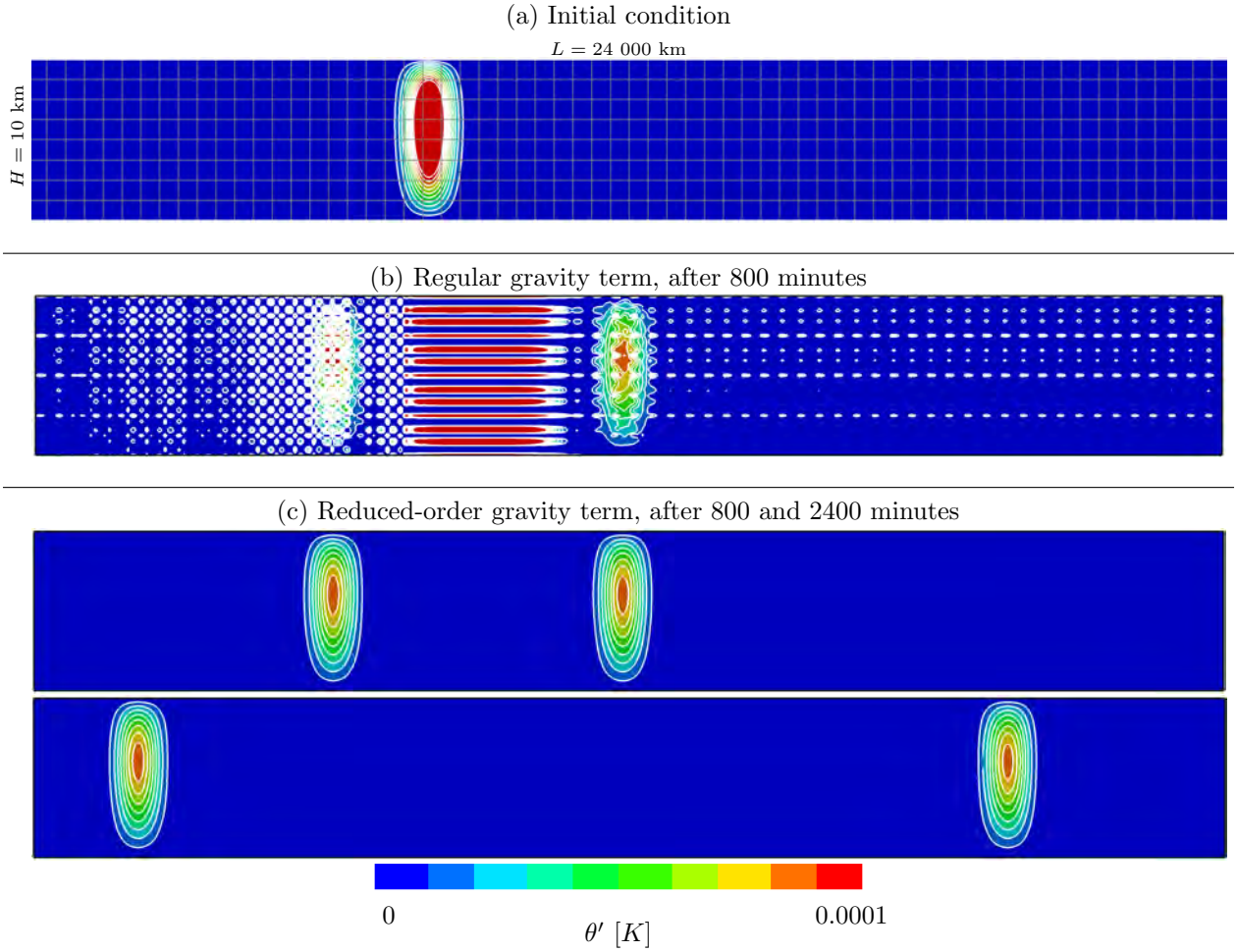

Figure 5: Gravity waves on an anisotropic mesh: potential temperature deviation θ'. The solution was computed using third-order polynomials on 64×8 elements (gray lines). Countour lines every 0.00001 K from 0.00001 K to 0.0001 K (white lines). For visualization purposes, the domain is vertically stretched by a factor of 320.

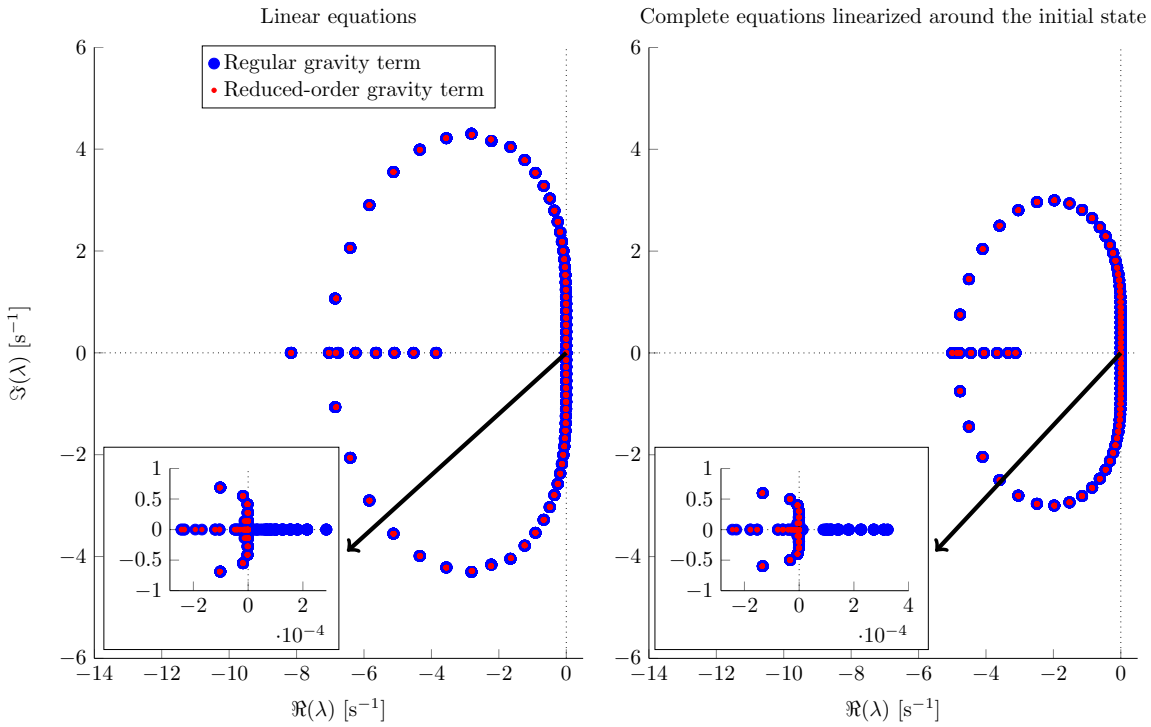

Figure 6: Gravity waves on an anisotropic mesh: eigenvalues λ of the discrete spatial operator for simulations with the regular gravity term (blue) and the reduced-order gravity term (red). This spatial operator corresponds to the linear equations (17) for the left plot and the complete equations (4) linearized around the initial condition for the plot on the right. The inner plots show a zoom for real parts of the eigenvalues lying around zero. The solution was computed using third-order polynomials on 8×8 elements.

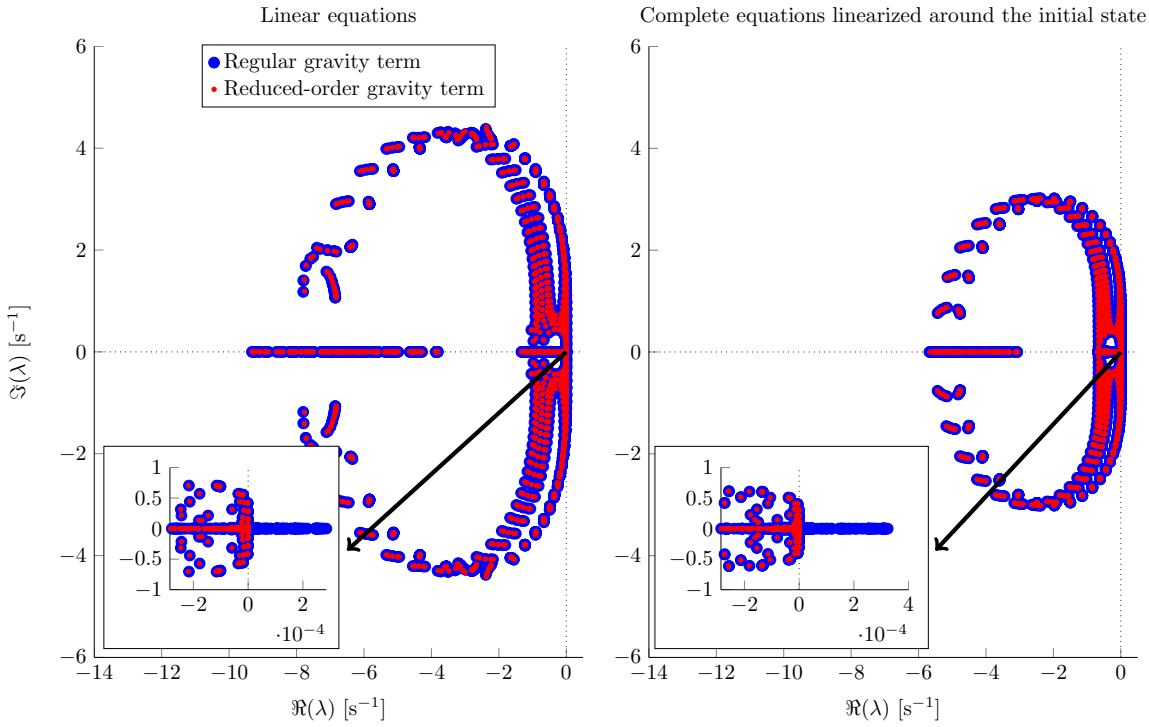

Figure 7: Original gravity waves test case from Baldauf and Brdar (2013): eigenvalues λ of the discrete spatial operator for simulations with the regular gravity term (blue) and the reduced-order gravity term (red). This spatial operator corresponds to the linear equations (17) for the left plot and the complete equations (4) linearized around the initial condition for the plot on the right. The inner plots show a zoom for real parts of the eigenvalues lying around zero. The solution was computed using third-order polynomials on 8×8 elements.

However, a question remains: why do those oscillations appear in the case of the anisotropic simulation only, while the height of the domain is the same for both configurations? The eigenvalues associated with the discrete spatial operators in the case of a regular mesh follow a similar pattern than the ones associated with the anisotropic mesh (Figure 7). In both cases, the operators are unstable for the regular gravity term, and the reduced-order gravity term removes the instability. However, because of the different scales involved, this instability is not always visible. For each setup, the gravity waves propagate at the same speed. By expanding significantly the horizontal dimensions in the anisotropic case, the time scale has been increased, resulting in much longer runs (i.e. 2400 minutes versus 30 minutes). The time for the waves to travel across the domain is then longer. This allows more time for the instabilities to develop. In contrast, with the isotropic run, the relatively fast dynamics hides the oscillations before they can grow significantly. Similar oscillations were observed when running the original gravity waves test case from Skamarock and Klemp (1994), modified in the same manner to obtain an anisotropic bubble in an anisotropic domain. In that case also, the vertical order reduction of the gravity term solved the problem, producing a solution without any spurious oscillation (not shown). A similar behaviour was also observed for simulations using high-order polynomials ($P = 8$).

The instability can be suppressed by having recourse to filtering or increasing the resolution. An increase of the resolution in not always possible, especially in a multi-resolution model for which the areas away from a region of interest are discretized with a coarse mesh. Filters have two main drawbacks. First, they usually rely upon parameters, needing to be tuned for the different applications, as well as spatial and temporal resolutions. Second, filtering is responsible for additional dissipation, which cannot be easily controlled. While the reduced-order gravity term is the source of numerical dissipation, it can be seen that this dissipation is lower than the one associated with the usual Boyd-Vandeven filter. To this aim, simulations of the anisotropic gravity waves have been performed. The numerical error regards to a reference solution has been computed using filtering or the reduced-order gravity term. The filter parameters are set to $s = \frac{2}{3}(P+1) = \frac{8}{3}$, which is a typical choice (Lauritzen et al., 2011), and several values of η decreasing until the model becomes unstable (Figure 8). The reference solution was computed using third-order polynomials on 256×32 elements, while the other simulations use the 64×8 elements mesh. To focus on the spatial error, an explicit time discretization with a sufficient small time step has been considered (0.05 seconds for the reference run and 0.2 seconds for the other simulations). It is seen in Figure 8 that, even for the lowest filtering ensuring stable simulations, the numerical error is always larger compared to simulations using the reduced-order gravity term. While realistic simulations will probably need additional filtering, a stable discretization with low numerical diffusivity allows for more control on the additional dissipation (e.g. through the use of selective filters). This additional flexibility will result in improved accuracy, especially in smooth resolved areas. While a loss of convergence is expected from the order reduction associated with the modified vertical discretization of the gravity term, a comparison with results presented in Figure 4 shows that the convergence is hardly affected (Figure 9). Because of its good properties, the modified scheme will be used for all the subsequent simulations presented in this section.

The temporal convergence of both the IMEX HV and IMEX V methods has been assessed on the gravity waves test case using a second-order time integration in combination with fifth order polynomial shape functions, ensuring the temporal error to be dominant. A unique mesh of 64×8 elements is used, and the simulations start with the maximum stable time step which is successively reduced by a factor of 2. In the convergence zone, the expected order 2 convergence is precisely attained, either for the IMEX HV and IMEX V methods (Figure 10). The global error stagnates when the temporal error reaches the same value as the spatial error.

6.2. Three-dimensional convergence

To assess the accuracy of the three-dimensional component of the model, a fully three-dimensional test case is needed, with a reference solution against which the results can be compared. Unfortunately, analytical solutions of three-dimensional nonhydrostatic flows are difficult to obtain. In order to estimate the convergence properties of the scheme, it is possible to solve the problem the other way around by having recourse to so-called manufactured solutions: an arbitrary solution is chosen, and source terms are added to the equations such that the assumed solution is actually the analytical solution of the problem.

For any prognostic variable field f, the solution is assumed to be of the form

$$f(x,y,z,t) = A^f \cos\left(\frac{2\pi}{L}x + \phi_x^f\right) \cos\left(\frac{2\pi}{L}y + \phi_y^f\right) \cos\left(\frac{2\pi}{H}z + \phi_z^f\right) \cos\left(\frac{2\pi}{T}t + \phi_t^f\right), \tag{34}$$

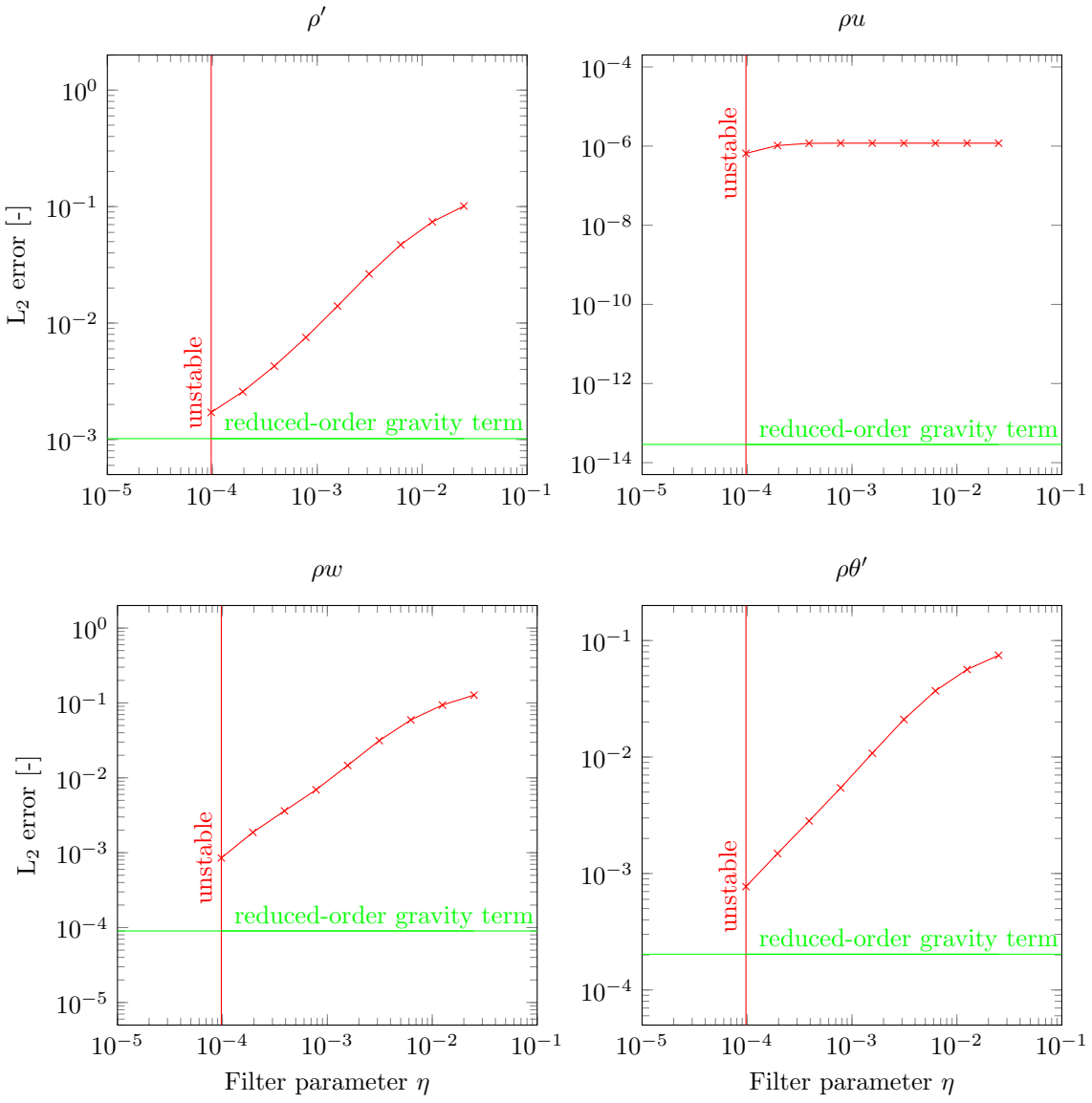

Figure 8: Gravity waves on an anisotropic mesh: L_2 error after 30 minutes for the prognostic variables, using the reduced-order gravity term (green), and the regular gravity term stabilized using a Boyd-Vandeven filter with several values of the parameter η (red). The vertical red lines corresponds to the minimum value of η under which the simulations are not stable (model crash).

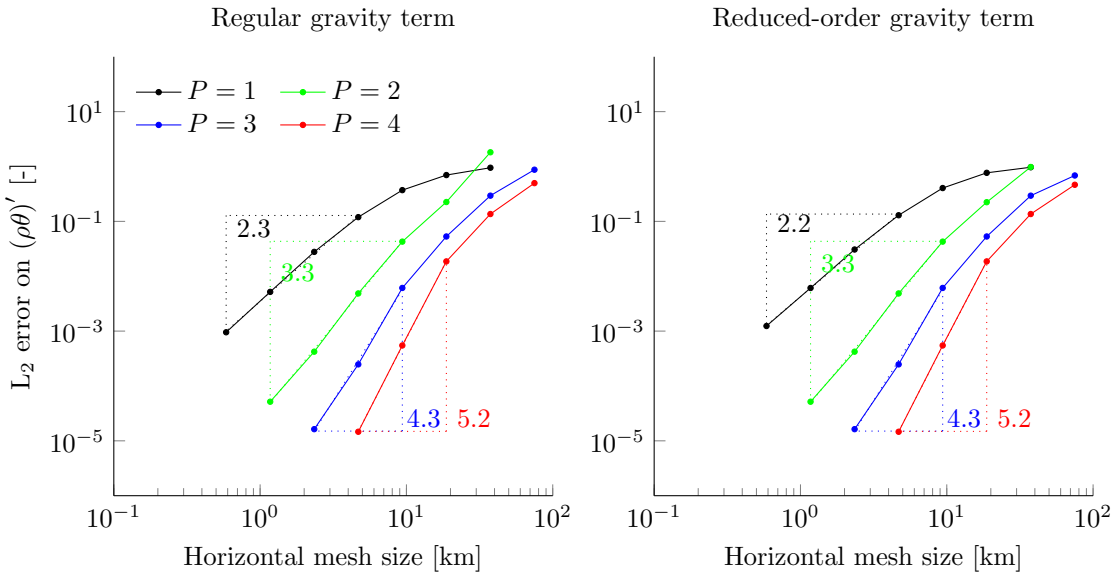

Figure 9: Gravity waves without and with vertical order reduction of the gravity term: spatial convergence of the L_2 error on $(\rho\theta)'$ after 30 minutes, using spatial polynomial orders P from 1 to 4.

f	A^f	ϕ_x^f	ϕ_y^f	ϕ_z^f	ϕ_t^f
ρ'	0.1	$2\pi\frac{2}{3}$	$2\pi\frac{5}{9}$	0	$2\pi\frac{6}{7}$
ρu	5	$2\pi\frac{6}{11}$	$2\pi\frac{5}{7}$	$\frac{3}{2}\pi$	$2\pi\frac{1}{5}$
ρv	3	$2\pi\frac{3}{5}$	$2\pi\frac{3}{8}$	$\frac{1}{2}\pi$	$2\pi\frac{2}{7}$
ρw	1	$2\pi\frac{3}{7}$	$2\pi\frac{11}{13}$	$\frac{3}{2}\pi$	$2\pi\frac{2}{7}$
$(\rho\theta)'$	0.1	$2\pi\frac{5}{11}$	$2\pi\frac{2}{5}$	π	$2\pi\frac{5}{6}$

Table 2: Parameters used for the analytical solution described by equation (34), with $L = H = 10000$ m and $T = 100$ s.

where L and H are respectively the horizontal and vertical dimensions of the domain while T is the total simulated time. This way, the prognostic variables describe a a complete wavelength along each dimension of the computational domain. The parameters for each of the variables are given in Table 2. The phases ϕ_z^f are chosen such that the lower and upper boundaries are compatible with wall boundary conditions. The lateral boundaries are periodic, allowing more freedom for the remaining parameters. The source terms to add to the equations such that the analytical solution is (34) have been found using the Symbolic Math Toolbox of Matlab[1].

For the different orders tested, the three-dimensional component of the model exhibits good convergence properties, as can be seen on Figure 11.

6.3. Density current

High-order discontinuous Galerkin methods may be subject to nonlinear aliasing errors, likely to generate spurious high-frequency oscillations. To prevent this noise from contaminating the solution, dissipation mechanisms may be needed in the case of practical applications (Jablonowski and Williamson, 2011). A good test case to evaluate those mechanisms is the density current benchmark, designed by Straka et al. (1993) and used to assess several non-hydrostatic atmospheric models (e.g. Giraldo and Restelli, 2008; Brdar et al., 2013). It consists in an initial cold bubble evolving in a neutral atmosphere at rest. The cold bubble

[1] `http://www.mathworks.nl/products/matlab`

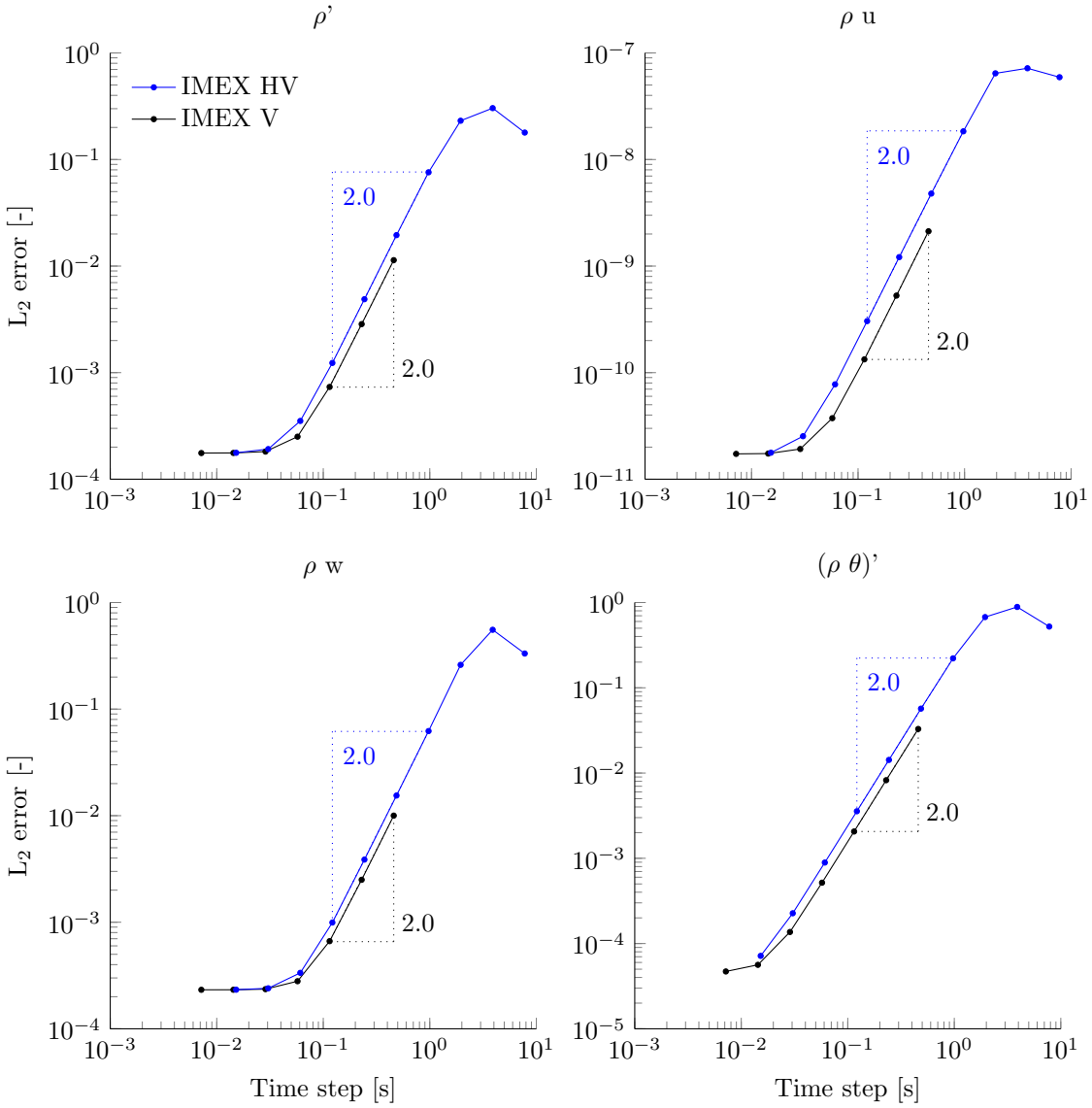

Figure 10: Gravity waves: temporal convergence of the L_2 error after 30 minutes for the prognostic variables, using respectively the second order IMEX HV and IMEX V time discetizations. Fifth order polynomials are used for the spatial discretization.

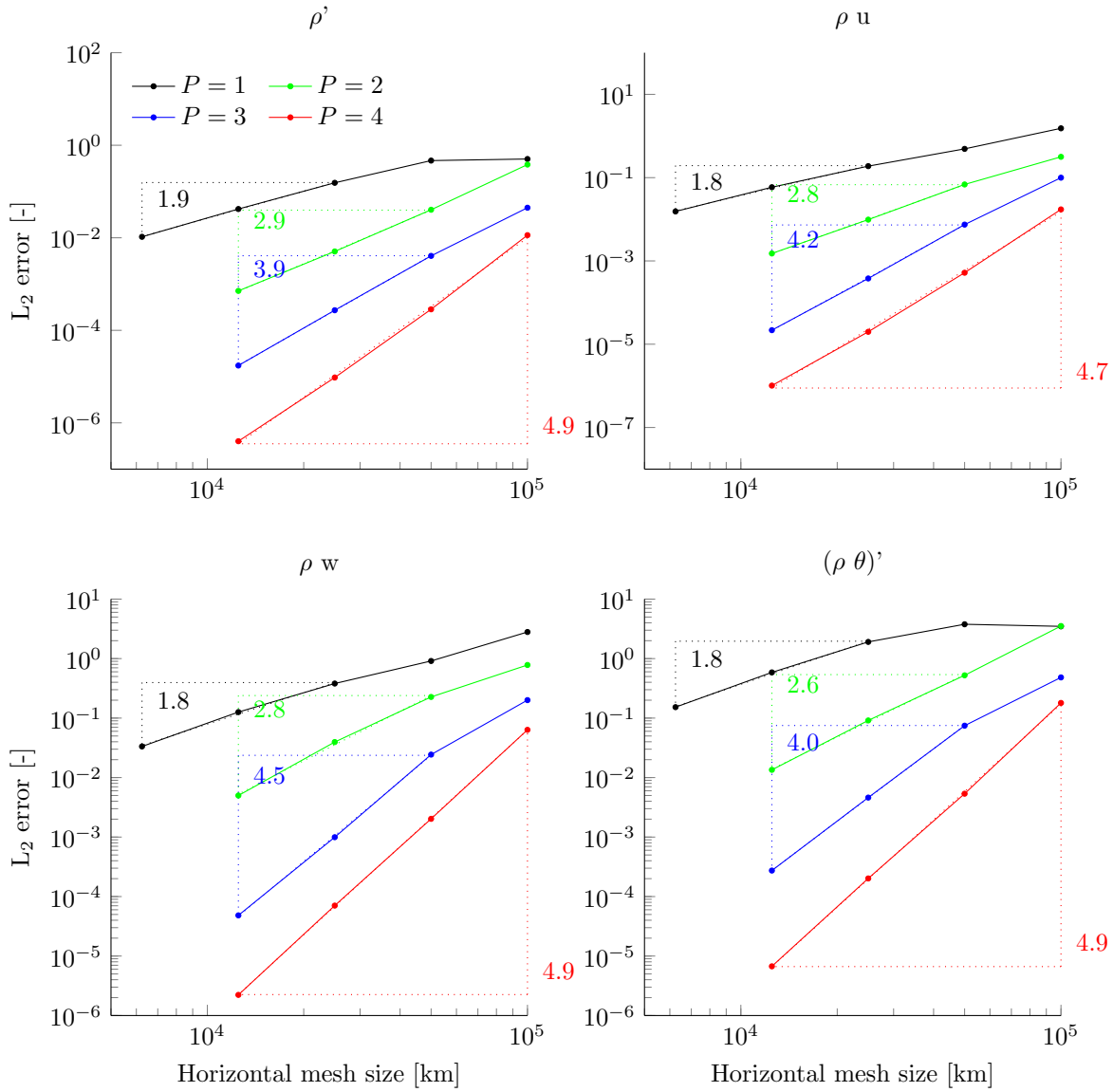

Figure 11: Three-dimensional box with analytical solution: spatial convergence of the L_2 error after $T = 100$ seconds for the prognostic variables, using spatial polynomial orders P from 1 to 4.

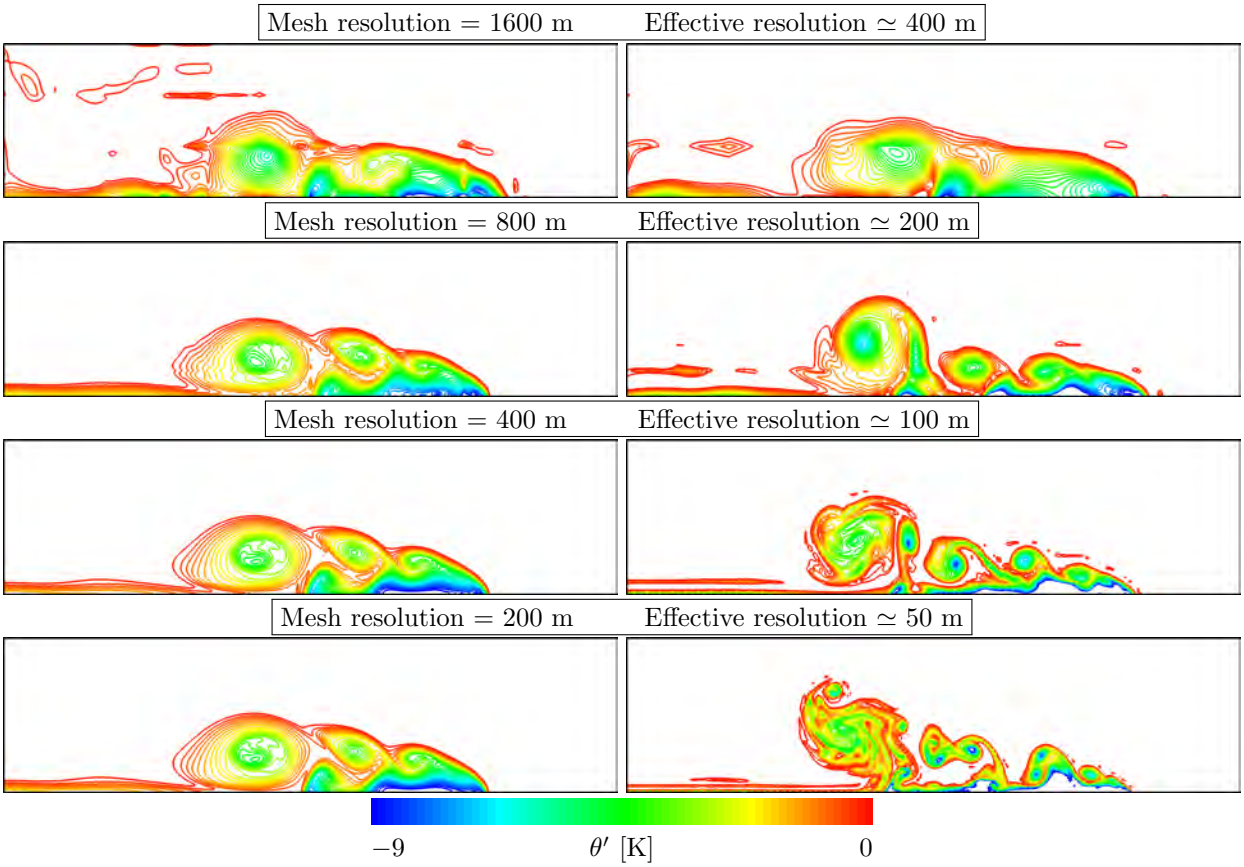

Figure 12: Density current: potential temperature perturbation θ' after 900 seconds at different resolutions using a background diffusion (left) or the Boyd-Vandeven filter (right). Contour lines every 0.25 K from -9 K to -0.25 K. Only a part of the domain is displayed, corresponding to the interval [0,19200] $\times$[0,4800] m.

initiates a downward density current which spreads out laterally along the lower boundary, forming Kelvin-Helmholtz shear instability rotors (Figure 12). The description of the test case can be found in Appendix B.

To allow for the computation of grid-converged numerical solutions, the original test case was designed with a background diffusion whose effect is to enforce a scale limit under which the flow cannot develop (Straka et al., 1993). For the purpose of this study, in addition to the classical test case with a background diffusion, a second simulation without diffusion has been run. The flow is not scale-limited anymore, and the simulation results become unresolved as smaller and smaller eddies are continuously generated. To prevent the apparition of excessive oscillations in this case, a Boyd-Vandeven filter with parameters $\eta = 0.2$ and $s = \frac{2}{3}(P+1) = \frac{8}{3}$ is applied after each time step. Such a simulation with no background diffusion is used to demonstrate the ability of the model to simulate accurately unresolved flows without generating spurious oscillations.

Simulations based on third-order polynomials for the spatial discretization have been run at different resolutions (Figures 12 and 13). The left columns of the figures show a numerical solution which is similar to the results of Giraldo and Restelli (2008), but some differences are seen. At 400 m resolution, two Kelvin-Helmholtz rotors are visible, and the second rotor is better resolved 200 m at resolution. However, the third rotor is already visible with a resolution of 200 m. Changing the resolution to 100 m slightly improves the results, decreasing the noise. The 50 m resolution simulation is almost identical to the 100 m resolution run, which is due to the fact that the test case is scale-limited by the constant diffusion term. The same conclusion can be drawn for the profile along 1 200 m height (Figure 13).

This result does not hold when no background diffusion is used: the test-case is not limited in scale anymore and an increase of resolution always results in an increase of flow complexity. This can be seen

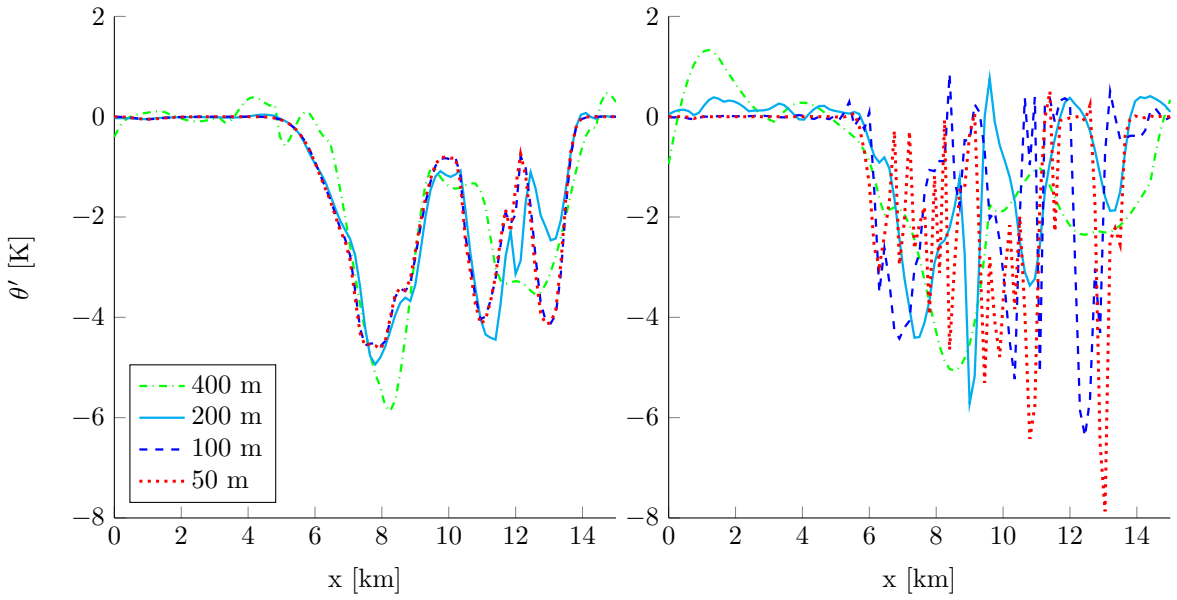

Figure 13: Density current: potential temperature perturbation θ' after 900 seconds at different resolutions using a background diffusion (left) or the Boyd-Vandeven filter (right). The figure displays profiles at the height $z = 1\ 200$ m.

on the right column of Figure 12, showing the model results obtained without diffusion term, but having recourse to the Boyd-Vandeven filter to stabilize the simulation. This is even more obvious on Figure 13 in which, rather to converging towards a solution, the finest resolution run produces strong and rapid fluctuations. While reproducing a known behaviour, these results also demonstrate the effectivity and robustness of the stabilization mechanisms for the simulation of complex unresolved flows in the absence of background diffusion.

6.4. Flows past mountains

To assess the model ability to represent nonhydrostatic flows and handle complex terrains, this section focuses on the simulation of flows past mountains. Such test cases have been widely used to validate nonhydrostatic models (Giraldo and Restelli, 2008; Brdar et al., 2013; Simarro et al., 2013). The definitions of the test cases considered in this section are described in Appendix C. They all consider a steady-state regime. In practice, the model is initiated with an unperturbed flow, and results are shown after 5 hours of physical time simulation, which has been verified to be long enough for the flow to reach a steady-state. For each of the mountain test cases, the orography is taken into account by a deformation of a rectangle mesh, whose elements are discretized using polynomials of the same order as the one used to discretize the prognostic variables (isoparametric elements). For the simulations of flows past mountains, radiative boundaries are implemented by using exterior value boundary conditions for which the prescribed state is the initial condition (i.e. the background flow). However, for the two-dimensional cases, a sponge layer was needed at the top boundary, characterized by $w_b = 7$ km and $\alpha = 0.01$. For the three-dimensional simulation, no sponge layer was necessary, the coarser resolution and boundary conditions being sufficient to damp the waves propagating towards the top.

The first benchmark is part of the test set devised by Skamarock et al. (2004), and has been specifically designed to evaluate the capability of a model to describe nonhydrostatic small-amplitude flows. An analytical solution has been derived, based on the linear mountain wave theory (Smith, 1979), and implemented in a Matlab code written by Giraldo and Restelli (2008). Because of the strong influence of boundary conditions, this test case is not optimal for convergence studies. However, the analytical solution is useful to validate the solution in the proximity of the mountain. Figure 14 shows the contours of simulated velocity compared to the analytical solution for a simulation using third-order polynomials on 133×33 elements, corresponding to approximate effective horizontal and vertical resolutions of respectively 360 m and 300 m. The IMEX HV time integration method has been used with a time step of 3.6 seconds. The model results are accurate close

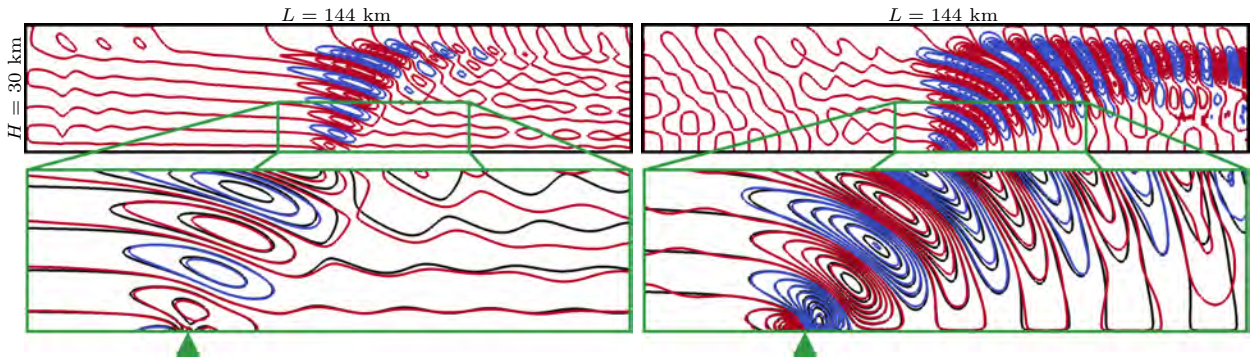

Figure 14: Flow past a nonhydrostatic mountain: numerical solution (blue negative, red positive) and analytical solution (black) after 5 hours. Contour lines for the horizontal velocity perturbation ($u - 10$ ms^{-1}) every 0.0025 ms^{-1} from -0.025 ms^{-1} to 0.025 ms^{-1} (left). Contour lines for the vertical velocity (w) every 0.0005 ms^{-1} from -0.005 ms^{-1} to 0.005 ms^{-1} (right). Solution computed using third-order polynomials on 133×33 elements, corresponding to approximate effective horizontal and vertical resolutions of respectively 360 m and 300 m. The green triangle indicates the location of the mountain.

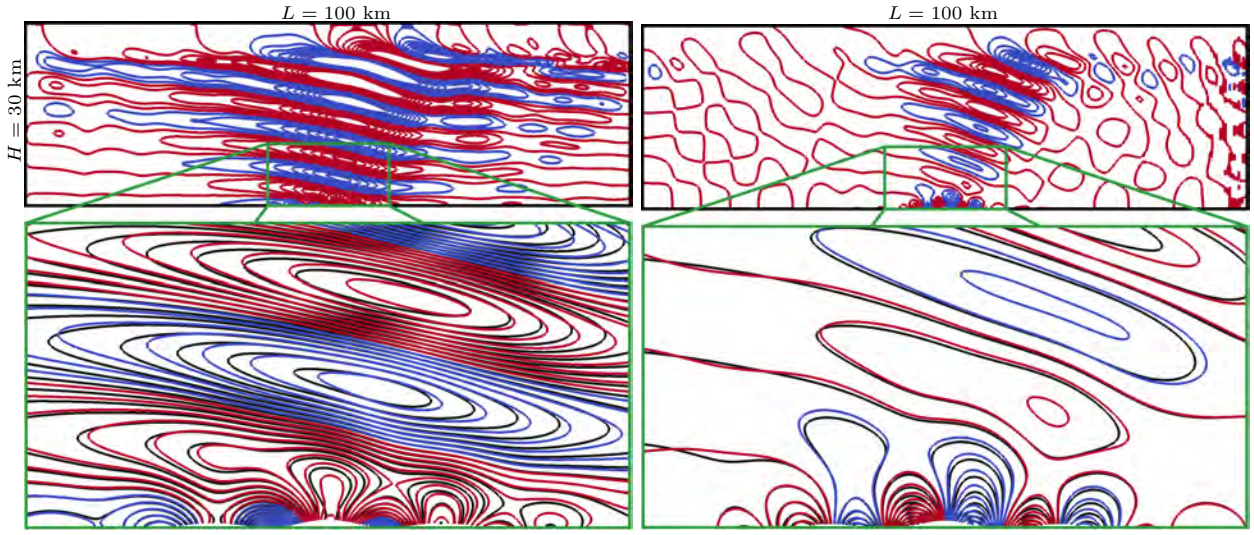

Figure 15: Schär mountain: numerical solution (blue negative, red positive) and analytical solution (black) after 5 hours. Contour lines for the horizontal velocity perturbation $u - 10$ ms^{-1} (left) and vertical velocity w (right) every 0.2 ms^{-1} from -0.2 ms^{-1} to 2 ms^{-1}. Solution computed using third-order polynomials on 133×47 elements, corresponding to approximate effective horizontal and vertical resolutions of respectively 250 m and 210 m.

to the mountain, but diverge from the analytical solution away from the mountain, due to the influence of the boundary conditions. The influence of nonhydrostatic effects is visible through the downstream tilt of the wave pattern associated with the vertical velocity, which cannot be catch by an hydrostatic model (Männik et al., 2003).

To validate the model behaviour in the case of complex terrain, we consider another test case describing an idealized flow past a mountain, originally developed by Schär et al. (2002). The analytical solution can be obtained in the same manner as for the nonhydrostatic mountain. Figure 15 shows the contours of simulated velocity compared to the analytical solution for a simulation using third-order polynomials on 133×47 elements, corresponding to approximate effective horizontal and vertical resolutions of respectively 250 m and 210 m. The IMEX HV time integration method has been used with a time step of 2.5 seconds. As for the nonhydrostatic mountain, the numerical results compare well with the analytical solution.

The last benchmark in this section is used to validate the three-dimensional component of the model. It consists of the simulation of a flow past a three-dimensional hydrostatic mountain. This test-case, already employed by Kelly and Giraldo (2012) to validate a three-dimensional discontinuous Galerkin model is an extension of the two-dimensional mountain test cases. An analytical solution along the plane of symmetry,

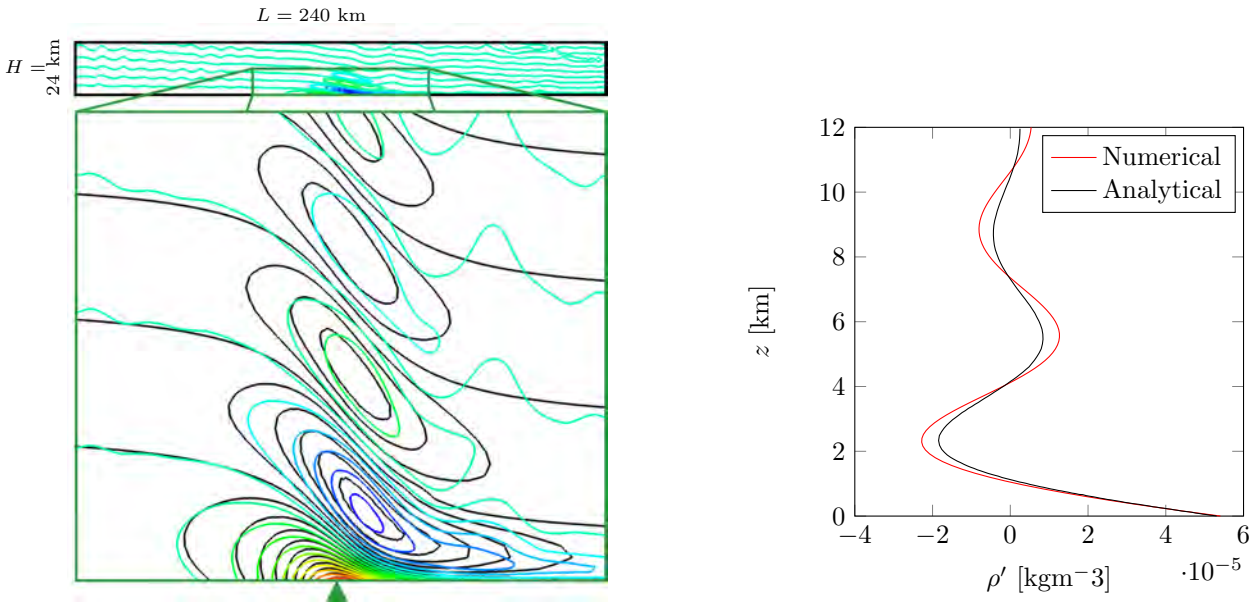

Figure 16: Flow past a three-dimensional linear hydrostatic mountain: density deviation ρ' after 5 hours. Left: contour lines every $5 \cdot 10^{-6}$ kgm^{-3} from $-2.5 \cdot 10^{-5}$ kgm^{-3} to $5.5 \cdot 10^{-5}$ kgm^{-3} for the model simulation (color) and analytical solution (black). Right: vertical profile at $x = y = 0$. Solution computed using third-order polynomials on $53 \times 53 \times 26$ elements, corresponding to approximate effective horizontal and vertical resolutions of respectively 1 500 m and 310 m. The green triangle indicates the location of the mountain.

based upon the linear Boussinesq approximation, has been made available thanks to the theory developed by Smith (1988) in isosteric coordinates.

The computational domain is discretized using $53 \times 53 \times 26$ third-order elements, corresponding to approximate effective horizontal and vertical resolutions of respectively 1 500 m and 310 m. Compared to the previous mountain benchmarks, this test case is characterized by a higher horizontal/vertical aspect ratio, fostering the IMEX V method, which has been used with a time step of 0.45 seconds. As for the previous test cases, the agreement with the analytical solution, based on a linear model, is very good close to the mountain, but deteriorates away from the mountain, due to the influence of the boundary conditions (Figure 16). The oscillations of density deviation around the zero value $\rho' = 0$ are likely due to the absence of boundary sponge layer and filtering mechanism.

7. Conclusions

In the continuity of published studies, a discontinuous Galerkin nonhydrostatic atmospheric model has been built and used for two- and three-dimensional simulations. To ensure stable simulations, the vertical order of the polynomial space used for the discretization of the gravity term has been reduced by one. While not affecting significantly the convergence properties of the scheme, this approach allowed the simulation of anisotropic flows without generating spurious oscillations, as it happened for the regular discretization. Those results are supported by a linear stability analysis, demonstrating that the use of this modified scheme discards the instability associated with the usual discretization. While filtering could have been used instead of the modified discretization, numerical results show that, in addition to the requirement of an additional parameter to be tuned, the use of filtering introduces a larger amount of numerical dissipation.

Validations against analytical solutions demonstrate the good convergence properties of the scheme, in accordance with the theoretical expectations. Dissipation mechanisms have been validated, as well as the scheme behavior in the case of unresolved flows, complex terrain or nonhydrostatic flows.

According to Giraldo et al. (2012), constructing scalable IMEX HV methods remains a challenge because such methods rely on iterative solvers and preconditioners. Thanks to the decoupling between columns, and the constantness of the system matrices, the IMEX time discretization with linear vertical terms implicit (IMEX V) can use direct solvers, and is supposed to be particularly efficient in the case of large-scale parallel

simulations. For high-resolution runs for which the anisotropy of the mesh is smaller, IMEX method with linear terms implicit (IMEX HV) or explicit methods may be more appropriate.

In the case of multi-resolution simulations, it would be interesting to study the coupling of different time integration methods, each one being applied to a different part of the computational domain. Other further developments should include dynamic mesh adaptivity, the resolution of the equations on the sphere for global simulations, as well as the implementation of parametrizations of simple physical processes.

Acknowledgements

The authors wish to thank Dr Michael Baldauf who derived the analytical solution for the gravity waves test case and provided the C code used to compute it. The authors also thank Professor Frank Giraldo for providing the Matlab routines for the computation of the analytical solution for the nonhydrostatic flow past a mountain and the Schär mountain. Sébastien Blaise and Jonathan Lambrechts are Postdoctoral Researchers with the Belgian Fund for Research (F.R.S.-FNRS), while Eric Deleersnijder is an honorary Research Associate with the same institution. Computational ressources were provided by the Consortium des Équipements de Calcul Intensif (CÉCI), funded by F.R.S.-FNRS under Grant No. 2.5020.11. Additional computing support from the National Center for Atmospheric Research (NCAR) has been made available through the project "Collaborative Research: A multiscale unified simulation environment for geoscientific applications", which is funded by the U.S.A. National Science Foundation under the Peta-apps grant number 0904599. The present study was carried out in the framework of the project "Taking up the challenges of multi-scale marine modeling" which is funded by the Communauté Française de Belgique under contract ARC 10/15-028.

Appendix A. Two-dimensional gravity waves in a channel

This gravity waves test case, for which an analytical solution is available, allows to analyze the order of convergence of the scheme without relying upon high-resolution solutions obtained either by the tested model or a different one. Its initial version was developed by Skamarock and Klemp (1994) and has been widely used for the validation of models. It consists of a channel in which gravity waves are triggered by an initial perturbation of the potential temperature in the form of a warm bubble. The waves then propagate towards the lateral boundaries. However, the original test case does not provide any analytical solution. Baldauf and Brdar (2013) recently proposed a slightly modified version, which allows to analytically derive the exact solution of the linearized compressible, non-hydrostatic Euler equations.

The computational domain is a vertical $x-z$ slice of the atmosphere of length $L = 300$ km and height $H = 10$ km with the bottom left corner as its origin. The initial atmosphere is described by a stably stratified state perturbed by a warm bubble. The hydrostatic background state reads:

$$\overline{\rho} = \rho_0 \exp(-\delta z), \tag{A.1}$$

$$\overline{\theta} = T_0 \exp(\delta z)^{\frac{R_d}{c_p}}, \tag{A.2}$$

$$\overline{p} = p_0 \exp(-\delta z), \tag{A.3}$$

with $\rho_0 = p_0\delta/g$ and $\delta = g/(R_d T_0)$. The background constant temperature T_0 is set to 250 K. According to Baldauf and Brdar (2013), the following constants are used: $R_d = 287.05$ Jkg^{-1}K^{-1}, $c_p = 1005$ Jkg^{-1}K^{-1} and $g = 9.80665$ ms^{-2}. A constant flow $\mathbf{u} = [20, 0]$ ms^{-1} is initially considered. The gravity waves are excited by an initial perturbation of the background state, corresponding to a warm bubble:

$$\rho' = \exp(-\delta z/2)\,\rho_b, \tag{A.4}$$

$$T' = \exp(\delta z/2)\,T_b, \tag{A.5}$$

$$p' = 0, \tag{A.6}$$

with

$$\rho_b = -\frac{p_0 T_b}{T_0^2 R_d}, \tag{A.7}$$

$$T_b = \Delta T \exp\left(-\frac{(x-x_c)^2}{d^2}\right)\sin(\frac{\pi z}{H}). \tag{A.8}$$

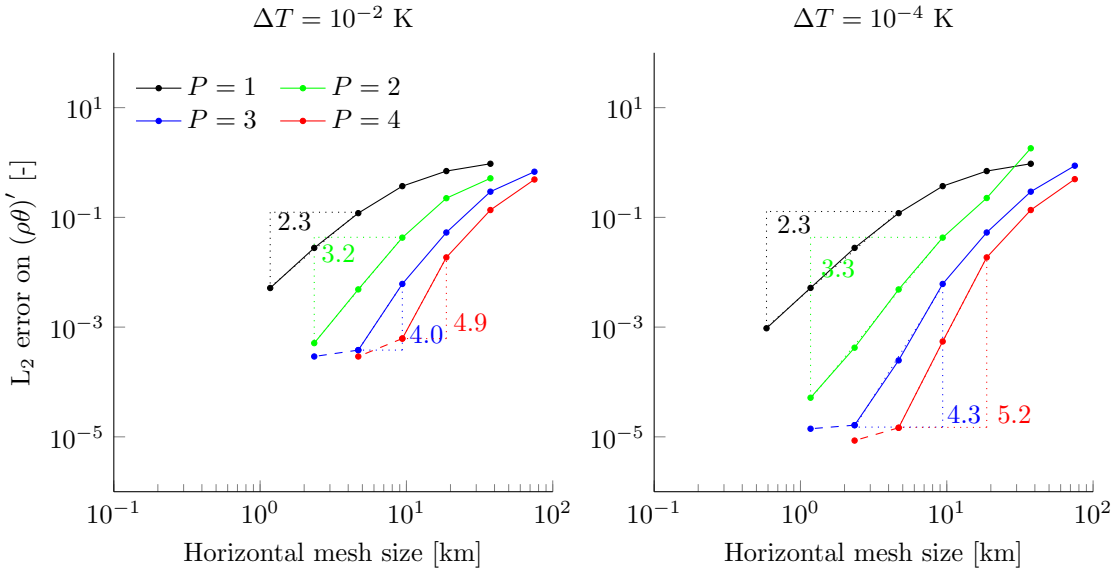

Figure A.17: Gravity waves with $\Delta T = 10^{-2}$ K and $\Delta T = 10^{-4}$ K: spatial convergence of the L_2 error on $(\rho\theta)'$ after 30 minutes, using spatial polynomial orders P from 1 to 4.

The temperature perturbation of the bubble ΔT is set to 0.01 K, while its position and width are defined by $x_c = 100$ km and $d = 5000$ m. The initial solution in terms of the model variable $\rho\theta$ can be obtained using:

$$\overline{\rho\theta} = \overline{\rho}\,\overline{\theta}, \tag{A.9}$$

$$(\rho\theta)' = (\overline{\rho} + \rho')\,(T_0 + T')\left(\frac{p_0}{\overline{p}}\right)^{\frac{R_d}{c_p}} - \overline{\rho\theta}. \tag{A.10}$$

Periodic boundary conditions are used on the lateral boundaries while free slip boundary conditions (i.e. zero vertical velocity) are enforced at the bottom and top boundaries.

Due to the linear approximation upon which the derivation of the analytical solution is based, there is a residual error in the analytical solution making model convergence stagnate at a certain level (e.g. dashed lines of Figure A.17). Decreasing the temperature perturbation to $\Delta T = 10^{-4}$ K produces very similar results in terms of convergence (Figure A.17), except that the error stagnates at a lower level due to the diminution of nonlinear effects. Note that, while only the error on $(\rho\theta)'$ is displayed on Figure A.17, a similar behaviour has been noticed for the other prognostic variables. To consider the analytical solution subject to the lowest approximation error, simulations presented in this article are performed with $\Delta T = 10^{-4}$ K.

Appendix B. Density current

Originally described by Straka et al. (1993), this test case consists in an initial cold bubble evolving in an atmosphere at rest of constant potential temperature $\theta_0 = 300$ K (neutral atmosphere). The cold bubble initiates a downward density current which spreads out laterally along the lower boundary, forming Kelvin-Helmholtz shear instability rotors. The initial state reads

$$\theta = \theta_0 + \frac{\theta_c}{2}\left(1 + \cos\left(\pi r\right)\right), \tag{B.1}$$

$$\rho = \frac{p_0}{\theta R_d}\left(1 - \frac{gz}{c_p\theta_0}\right)^{\frac{c_v}{R_d}}, \tag{B.2}$$

with

$$r = \min\left(1\ ,\ \sqrt{\left(\frac{x - x_c}{x_r}\right)^2 + \left(\frac{z - z_c}{z_r}\right)^2}\right) \tag{B.3}$$

as well as $\theta_c = -15$ K, $x_c = 0$, $z_c = 3$ km, $x_r = 4$ km and $z_r = 2$ km. The following constants are considered: $g = 9.80616$ ms^{-1}, $R_d = 287$ Jkg^{-1}K^{-1}, $c_v = 717.5$ Jkg^{-1}K^{-1} and $c_p = 1004.5$ Jkg^{-1}K^{-1}.

Wall (free slip) conditions are considered for all four boundaries. To allow for the computation of grid-converged numerical solutions, the original test case was designed with a background diffusion $\kappa = 75$ m^{2}s^{-1}, whose effect is to enforce a scale limit under which the flow cannot develop.

Appendix C. Flows past mountains

Appendix C.1. Linear nonhydrostatic mountain

This test case has been designed by Skamarock et al. (2004) to assess the ability of a model to describe nonhydrostatic small-amplitude flows. The computational domain is a vertical $x - z$ slice of the atmosphere with the bottom left corner as its origin, of length 144 km and height 30 km. The bottom boundary elevation z_b is perturbed by a mountain of height $h_c = 1$ m and horizontal scale $a_c = 1$ km, centered at $x_c = 72$ km:

$$z_b = \frac{h_c}{1 + \left(\frac{x - x_c}{a_c}\right)^2}. \tag{C.1}$$

The model is started with a hydrostatic unperturbed flow defined by:

$$\theta = \theta_0 \exp\left(\frac{N^2 z}{g}\right), \tag{C.2}$$

$$\rho = \frac{p_0}{\theta R_d}\left(1 + \frac{g^2\left(\exp\left(-\frac{N^2 z}{g}\right) - 1\right)}{c_p \theta_0 N^2}\right)^{\frac{c_v}{R_d}}, \tag{C.3}$$

where $N = 0.01$ s^{-1} is the Brunt-Väisälä frequency and $\theta_0 = 280$ K. The constants g, R_d, c_v and c_p, take the same values as for the density current benchmark (Appendix B). A initial constant velocity is considered, which is horizontal: $\mathbf{u} = [10, 0]$ ms^{-1}.

A free-slip condition is employed at the bottom boundary, while non-reflecting conditions need to be used for the lateral and top boundaries.

Appendix C.2. Schär mountain

For this test case, proposed by Schär et al. (2002) the setup is the same as for the linear nonhydrostatic mountain benchmark, except that the domain length is $L = 100$ km, and the orography is more complex, representing a five-peak mountain chain:

$$z_b = h_c \exp\left(-\left(\frac{x}{a_c}\right)^2\right) \cos^2\left(\frac{\pi(x - x_c)}{\lambda_c}\right) \tag{C.4}$$

with $h_c = 250$ m, $\lambda_c = 4$ km, $a_c = 5$ km and $x_c = 50$ km.

Appendix C.3. Linear hydrostatic 3d mountain

This test-case, already employed by Kelly and Giraldo (2012) to validate a three-dimensional discontinuous Galerkin model is an extension of the two-dimensional mountain test cases. An analytical solution of the linear problem is available along the plane of symmetry, thanks to the theory developed by Smith (1988) in isosteric coordinates.

The configuration is similar to the two-dimensional mountain test cases, except that a three-dimensional domain of horizontal size 240×240 km and height 24 km is considered, in which the bottom elevation reads:

$$z_b = \frac{h_c}{\left(1 + \left(\frac{x - x_c}{a_c}\right)^2 + \left(\frac{y - y_c}{a_c}\right)^2\right)^{\frac{3}{2}}}, \tag{C.5}$$

with $x_c = y_x = 120$ km and $h_c = 1$ m. A constant Brunt-Väisälä frequency $N = \frac{g}{\sqrt{c_p \theta_0}}$ s^{-1} with $\theta_0 = 250$ K is considered. The initial background velocity is constant and horizontal: $\mathbf{u} = [20, 0, 0]$ ms^{-1}.

References

Adjerid, S., Baccouch, M., 2007. The Discontinuous Galerkin Method for Two-Dimensional Hyperbolic Problems. Part I: Superconvergence Error Analysis. Journal of Scientific Computing 33, 75–113.

Arnold, D., 1982. An interior penalty finite element method with discontinuous elements. SIAM Journal on Numerical Analysis 19, 742–760.

Arnold, D.N., Brezzi, F., Cockburn, B., Marini, L.D., 2002. Unified analysis of discontinuous Galerkin methods for elliptic problems. SIAM Journal on Numerical Analysis 39, 1749–1779. doi:10.1137/S0036142901384162.

Ascher, U.M., Ruuth, S.J., Spiteri, R.J., 1997. Implicit-explicit Runge-Kutta methods for time-dependent partial differential equations. Applied Numerical Mathematics 25, 151–167. doi:10.1016/S0168-9274(97)00056-1.

Ascher, U.M., Ruuth, S.J., Wetton, B.T., 1995. Implicit-explicit methods for time-dependent partial differential equations. SIAM Journal on Numerical Analysis 32, 797–823. doi:10.1137/0732037.

Baldauf, M., Brdar, S., 2013. An analytic solution for linear gravity waves in a channel as a test for numerical models using the non-hydrostatic, compressible euler equations. Quarterly Journal of the Royal Meteorological Society , accepted for publication,doi:10.1002/qj.2105.

Blaise, S., Comblen, R., Legat, V., Remacle, J., Deleersnijder, E., Lambrechts, J., 2010. A discontinuous finite element baroclinic marine model on unstructured prismatic meshes. Part I: Space discretization. Ocean Dynamics 60, 1371–1393.

Blaise, S., Lambrechts, J., Deleersnijder, E., 2015. Stereographic projection for three-dimensional global discontinuous Galerkin atmospheric modeling. Journal of Advances in Modeling the Earth System 7.

Blaise, S., St-Cyr, A., 2012. A dynamic *hp*-adaptive discontinuous Galerkin method for shallow water flows on the sphere with application to a global tsunami simulation. Monthly Weather Review 140, 978–996.

Botta, N., Klein, R., Langenberg, S., Lützenkirchen, S., 2004. Well balanced finite volume methods for nearly hydrostatic flows. Journal of Computational Physics 196, 539–565.

Boyd, J.P., 1996. The erfc-log filter and the asymptotics of the euler and vandeven sequence accelerations, in: A.V. Ilin, L.S. (Ed.), Proceedings of the Third International Conference on Spectral and High Order Methods, pp. 267–275.

Brdar, S., Baldauf, M., Dedner, A., Klöfkorn, R., 2013. Comparison of dynamical cores for NWP models: comparison of COSMO and dune. Theoretical and Computational Fluid Dynamics 27, 453–472.

Cockburn, B., Karniadakis, G.E., Shu, C.W., 1999. The development of discontinuous Galerkin methods.

Cockburn, B., Shu, C., 1998a. The local discontinuous Galerkin finite element method for time-dependent convection-diffusion systems. SIAM Journal on Numerical Analysis 35, 2440–2463. doi:10.1137/S0036142997316712.

Cockburn, B., Shu, C.W., 1998b. The rungekutta discontinuous galerkin method for conservation laws v: Multidimensional systems. Journal of Computational Physics 141, 199–224.

Comblen, R., Blaise, S., Legat, V., Remacle, J., Deleersnijder, E., Lambrechts, J., 2010. A discontinuous finite element baroclinic marine model on unstructured prismatic meshes. Part II: Implicit/explicit time discretization. Ocean Dynamics 60, 1395–1414.

Dennis, J., Fournier, A., Spotz, W.F., St-Cyr, A., Taylor, M.A., Thomas, S.J., Tufo, H., 2005. High-Resolution Mesh Convergence Properties and Parallel Efficiency of a Spectral Element Atmospheric Dynamical Core. International Journal of High Performance Computing Applications 19, 225–235.

Dennis, J.M., Edwards, J., Evans, K.J., Guba, O., Lauritzen, P.H., Mirin, A.A., St-Cyr, A., Taylor, M.A., Worley, P.H., 2012. CAM-SE: a scalable spectral element dynamical core for the community atmosphere model. International Journal of High Performance Computing Applications 26, 74–89.

Dolejší, V., Feistauer, M., 2004. A semi-implicit discontinuous galerkin finite element method for the numerical solution of inviscid compressible flow. Journal of Computational Physics 198, 727–746.

Durran, D.R., Klemp, J.B., 1983. A compressible model for the simulation of moist mountain waves. Monthly Weather Review 111, 2341–2361.

Giraldo, F.X., Kelly, J., Constantinescu, E., 2012. Implicit-explicit formulations of a three-dimensional nonhydrostatic unified model of the atmosphere (NUMA). SIAM Journal on Scientific Computing 35, B1162–B1194.

Giraldo, F.X., Restelli, M., 2008. A study of spectral element and discontinuous Galerkin methods for mesoscale atmospheric modeling: equation sets and test cases. Journal of Computational Physics 227, 3849–3877.

Giraldo, F.X., Restelli, M., Lauter, M., 2010. Semi-implicit formulations of the navier-stokes equations: Application to nonhydrostatic atmospheric modeling. SIAM Journal on Scientific Computing 32, 3394–3425.

Gopalakrishnan, S., Bacon, D., Ahmad, N., Boybeyi, Z., Dunn, T., Hall, M., Jin, Y., Lee, P., Mays, D., Madala, R., et al., 2002. An operational multiscale hurricane forecasting system. Monthly Weather Review 130, 1830–1847.

Hamilton, K., 2008. High Resolution Numerical Modelling of the Atmosphere and Ocean. Springer. chapter Numerical Resolution and Modeling of the Global Atmospheric Circulation: A Review of Our Current Understanding and Outstanding Issues. pp. 7–27.

Hesthaven, J.S., Wartburton, T., 2008. Nodal Discontinuous Galerkin Methods. Algorithms, Analysis and Applications. volume 54 of *Texts in Applied Mathematics*. Springer, Berlin.

IPCC, 1997. Special Report. The Regional Impacts of Climate Change: An Assessment of Vulnerability.

Jablonowski, C., Williamson, D.L., 2011. The Pros and Cons of Diffusion, Filters and Fixers in Atmospheric General Circulation Models, in: Lauritzen, P., Jablonowski, C., Taylor, M., Nair, R. (Eds.), Numerical Techniques for Global Atmospheric Models. Springer Berlin Heidelberg. number 80 in Lecture Notes in Computational Science and Engineering, pp. 381–493.

Karniadakis, G.E., Sherwin, S.J., 2005. Spectral/hp Element Methods for Computational Fluid Dynamics (Numerical Mathematics and Scientific Computation). Oxford University Press, USA.

Kelly, J.F., Giraldo, F.X., 2012. Continuous and discontinuous galerkin methods for a scalable three-dimensional nonhydrostatic atmospheric model: Limited-area mode. Journal of Computational Physics 231, 7988–8008.

Krivodonova, L., 2007. Limiters for high-order discontinuous galerkin methods. Journal of Computational Physics 226, 879–896.

Lauritzen, P., Jablonowski, C., Taylor, M., Nair, R., 2011. Numerical Techniques for Global Atmospheric Models. Springer.

Lin, Y.L., 2010. Mesoscale Dynamics - Atmospheric science and meteorology. Cambridge University Press.

Lindzen, R.S., Fox-Rabinovitz, M., 1989. Consistent Vertical and Horizontal Resolution. Monthly Weather Review 117, 2575–2583. URL: http://journals.ametsoc.org/doi/abs/10.1175/1520-0493%281989%29117%3C2575%3ACVAHR%3E2.0.CO%3B2, doi:10.1175/1520-0493(1989)117<2575:CVAHR>2.0.CO;2.

Machenhauer, B., Kaas, E., Lauritzen, P., 2009. Computational Methods for the Atmosphere and the Oceans: Special Volume. volume 14. Elsevier.

Männik, A., Rõõm, R., Luhamaa, A., 2003. Nonhydrostatic generalization of a pressure-coordinate-based hydrostatic model with implementation in HIRLAM: validation of adiabatic core. Tellus A 55, 219–231.

McClean, J.L., Bader, D.C., Bryan, F.O., Maltrud, M.E., Dennis, J.M., Mirin, A.A., Jones, P.W., Kim, Y.Y., Ivanova, D.P., Vertenstein, M., Boyle, J.S., Jacob, R.L., Norton, N., Craig, A., Worley, P.H., 2011. A prototype two-decade fully-coupled fine-resolution CCSM simulation. Ocean Modelling 39, 10–30.

McMorrow, D., 2013. Technical Challenges of Exascale Computing. MITRE Corporation.

Nair, R., Thomas, S., Loft, R., 2005. A discontinuous Galerkin global shallow water model. Monthly Weather Review 133, 876–888.

Nair, R.D., Choi, H.W., Tufo, H.M., 2009. Computational aspects of a scalable high-order discontinuous galerkin atmospheric dynamical core. Computers & Fluids 38, 309–319.

Palipane, E., Lu, J., Chen, G., Kinter, J.L., 2013. Improved annular mode variability in a global atmospheric general circulation model with 16 km horizontal resolution. Geophysical Research Letters 40, 4893–4899.

Park, S.H., Skamarock, W.C., Klemp, J.B., Fowler, L.D., Duda, M.G., 2013. Evaluation of global atmospheric solvers using extensions of the jablonowski and williamson baroclinic wave test case. Monthly Weather Review 141, 3116–3129.

Persson, P.O., Peraire, J., 2006. Sub-cell shock capturing for discontinuous galerkin methods, in: 44th AIAA Aerospace Sciences Meeting and Exhibit. American Institute of Aeronautics and Astronautics, pp. 1–14.

Rauscher, S.A., Ringler, T.D., Skamarock, W.C., Mirin, A.A., 2013. Exploring a global multiresolution modeling approach using aquaplanet simulations*. Journal of Climate 26, 2432–2452.

Restelli, M., Giraldo, F.X., 2009. A conservative discontinuous galerkin semi-implicit formulation for the navierstokes equations in nonhydrostatic mesoscale modeling. SIAM Journal on Scientific Computing 31, 2231–2257.

Riviere, B., 2008. Discontinuous Galerkin Methods for Solving Elliptic and Parabolic Equations: Theory and Implementation. volume 35 of *Frontiers in Mathematics*. SIAM.

Runge, C., 1901. über empirische funktionen und die interpolation zwischen quidistanten ordinaten. Zeitschrift für Mathematik und Physik 46, 224–243.

Schär, C., Leuenberger, D., Fuhrer, O., Lüthi, D., Girard, C., 2002. A new terrain-following vertical coordinate formulation for atmospheric prediction models. Monthly Weather Review 130, 2459–2480.

Shahbazi, K., 2005. An explicit expression for the penalty parameter of the interior penalty method. Journal of Computational Physics 205, 401–407. doi:10.1016/j.jcp.2004.11.017.

Shukla, J., Hagedorn, R., Miller, M., Palmer, T.N., Hoskins, B., Kinter, J., Marotzke, J., Slingo, J., 2009. Strategies: Revolution in climate prediction is both necessary and possible: A declaration at the world modelling summit for climate prediction. Bulletin of the American Meteorological Society 90, 175–178.

Simarro, J., Homar, V., Simarro, G., 2013. A non-hydrostatic global spectral dynamical core using a height-based vertical coordinate. Tellus A 65.

Skamarock, W.C., Doyle, J.C., Clark, P., Wood, N., 2004. A standard test set for nonhydrostatic dynamical cores of nwp models. Poster presented at the 16th Conference on Numerical Weather Prediction, Seattle, WA.

Skamarock, W.C., Klemp, J.B., 1994. Efficiency and Accuracy of the Klemp-Wilhelmson Time-Splitting Technique. Monthly Weather Review 122, 2623–2630.

Slingo, J., Bates, K., Nikiforakis, N., Piggott, M., Roberts, M., Shaffrey, L., Stevens, I., Vidale, P.L., Weller, H., 2009. Developing the next-generation climate system models: challenges and achievements. Philosophical Transactions of the Royal Society A: Mathematical, Physical and Engineering Sciences 367, 815–831.

Smith, R.B., 1979. The influence of mountains on the atmosphere. Advances in Geophysics 21, 87–230.

Smith, R.B., 1988. Linear theory of stratified flow past an isolated mountain in isosteric coordinates. Journal of the Atmospheric Sciences 45, 3889–3896.

St-Cyr, A., Neckels, D., 2009. A fully implicit Jacobian-free high-order discontinuous Galerkin mesoscale flow solver. Computational Science-ICCS , 243–252.

Steppeler, J., Bitzer, H.W., Minotte, M., Bonaventura, L., 2002. Nonhydrostatic atmospheric modeling using a z-coordinate representation. Monthly Weather Review 130, 2143–2149.

Straka, J.M., Wilhelmson, R.B., Wicker, L.J., Anderson, J.R., Droegemeier, K.K., 1993. Numerical solutions of a non-linear density current: A benchmark solution and comparisons. International Journal for Numerical Methods in Fluids 17, 1–22.

Süli, E., Mayers, D.F., 2003. An Introduction to Numerical Analysis. Cambridge University Press, Cambridge ; New York.

Taylor, M., Tribbia, J., Iskandarani, M., 1997. The spectral element method for the shallow water equations on the sphere. Journal of Computational Physics 130, 92–108.

Teschl, G., 2012. Ordinary Differential Equations and Dynamical Systems. American Mathematical Society, Providence, R.I.

Thuburn, J., 2015. NUMERICAL MODELS | Methods, in: Zhang, G.R.N.P. (Ed.), Encyclopedia of Atmospheric Sciences (Second Edition). Academic Press, Oxford, pp. 161–166. URL: http://www.sciencedirect.com/science/article/pii/B9780123822253002462.

Thunis, P., Borstein, R., 1996. Hierarchy of Mesoscale Flow Assumptions and Equations. Journal of the Atmospheric Sciences 53, 380–397.

Wehner, M., 2008. Towards Ultra-High Resolution Models of Climate and Weather. International Journal of High Performance Computing Applications 22, 149–156.

Weller, H., Lock, S.J., Wood, N., 2013. Runge-kutta IMEX schemes for the horizontally explicit/vertically implicit (HEVI) solution of wave equations. Journal of Computational Physics 252, 365–381. doi:10.1016/j.jcp.2013.06.025.

Weller, H., Weller, H.G., Fournier, A., 2009. Voronoi, delaunay, and block-structured mesh refinement for solution of the shallow-water equations on the sphere. Monthly Weather Review 137, 4208–4224.